
FACULTY OF TECHNOLOGY

# DOUBLE WHEEL CRUSHER PROTOTYPE

Janne Torvela

DEGREE PROGRAM OF MECHANICAL ENGINEERING

Master's thesis

February 2020

# ABSTRACT

Double Wheel Crusher prototype

Janne Torvela

University of Oulu, Degree Program of Mechanical Engineering

Master's thesis 2020, 70 pp. + 2 Appendixes

Supervisor(s) at the university: Dr. Toni Liedes, Dr. Marcos de Paiva Bueno

This thesis presents a proof of concept for a new testing device. The prototype device was commissioned as a part of a project to develop a fast, low-cost, and reliable breakage characterization test for geo-metallurgical modelling. One of the key processes involved in minerals extraction is comminution: mineral ores are broken down with crushing and grinding machinery. Comminution testing can be used for the purposes of optimizing these processes. Various testing methods used in the industry subject rock particles to varying levels of crushing impact to measure the amount of fine materials liberated relative to the input energy. The role of mechatronic engineering in this context is to design and develop intelligent machines that ease the work of the researchers and technicians performing these tests.

The structure of the new device was proposed as a variation of an instrumented roll crusher with an adjustable gap. The trial operation of the prototype was done using rocks from different mine sites around Finland. The test set resulted in data with a clearly identifiable correspondence of energy to the amount of breakage, proving the plausibility of the device. Some issues were found with the accuracy of energy measurements. The programming error behind the fault was corrected and the improved device was found to produce a standard deviation of measurement of 1.07 Joules. Means to further improve the accuracy of the energy and force measurements are discussed, with recommendations and suggestions for other improvements to the device in the future.

*Keywords: crushing machinery, research equipment, mining industry*

# TIIVISTELMÄ

Kaksoispyörämurskaimen prototyyppi

Janne Torvela

Oulun Yliopisto, Konetekniikan tutkinto-ohjelma

Diplomityö 2020, 70 s. + 2 liitettä

Työn ohjaaja(t) yliopistolla: TkT Toni Liedes, Dr. Marcos de Paiva Bueno

Tässä työssä koetetaan uuden mittauslaiteen konseptia. Prototyyppilaite tilattiin osana projektia, jonka tarkoituksena on kehittää uusi nopea, varma, ja edullinen menetelmä mineraalien hienontumisen testaamiseen geometallurgisen mallinnuksen tarpeisiin. Eräs mineraalien louhinnan ja jalostamisen keskeisistä prosesseista on malmin hienontaminen murskaus- ja jauhatuskoneilla. Hienonnustestausta voidaan hyödyntää näiden prosessien optimointiin. Kaivosteollisuudessa käytetyissä testausmenetelmissä kivipartikkeleihin kohdistetaan erisuuruisia iskuvoimia, joiden hienonnusvaikutusta mitataan suhteessa syötetyn energian määrään. Mekatronisen suunnittelun tehtävä tässä yhteydessä on kehittää älykkäitä laitteita helpottamaan näitä kokeita suorittavien tutkijoiden ja teknikkojen työtä.

Uuden laitteen rakenne mukailee telamurskaimen toimintaperiaatetta. Prototyyppiä testattiin murskaamalla eri puolelta Suomea tuotuja kivinäytteitä. Testin tuloksista on selvästi tunnistettavissa käytetyn energian vaikutus murtumismäärään. Testien aikana havaittiin ongelmia energiamittauksen tarkkuudessa. Vian aiheuttanut ohjelmointivirhe korjattiin ja parannellun laitteiston mittaustuloksen hajonnaksi todettiin 1,07 Joulea. Työn lopussa esitetään ehdotuksia energian ja voiman mittaustarkkuuden parantamiseksi, sekä muita mahdollisia parannuksia laitteen jatkokehitystä varten.

*Asiasanat: murskauskoneet, tutkimuslaitteet, kaivosteollisuus*

# PREFACE

This thesis is about designing, building and testing a prototype machine for an improved means of rock comminution testing. The practical portions of this work were done during the spring and summer of 2019 with some of the testing work extending over the autumn period.

I'd like to thank Dr. Marcos de Paiva Bueno and Dr. Toni Liedes for the opportunity to work on this project, Tabatha Chavez Matus for her help and feedback as a test user for the machine, and Ville Pirnes for his helpful instructions regarding strain gauge sensors. Furthermore, I'd like to thank Kasper Hahtonen, Tapani Mäntykenttä, Pasi Heikkinen and Kaarlo Vähätaini, as well as the rest of the machine shop crew, for their excellent work and assistance in manufacturing and building the prototype.

Oulu, 13.2.2020

*Janne Torvela*
Janne Torvela

# TABLE OF CONTENTS

# ABBREVIATIONS AND NOTATIONS

| | |
|---|---|
| A | asymptote of the comminution energy curve |
| AC | alternating Current |
| BLDC | brushless direct current motor |
| b | exponential coefficient of the comminution energy curve |
| CAD | computer aided design |
| DC | direct current |
| $D_W$ | wheel diameter |
| DWT | drop weight test |
| d | maximum equivalent feed particle size |
| E | energy of comminution |
| GRBT | geomet rolls breakage test |
| $K_d$ | derivative control coefficient |
| $K_i$ | integral control coefficient |
| $K_p$ | proportional control coefficient |
| LabVIEW | laboratory virtual instrument engineering workbench (NI) |
| MATLAB | matrix laboratory; a numerical computing environment by MathWorks |
| NI | National Instruments |
| n | breakage products size fraction |
| PETG | polyethylene terephthalate glycol; a thermoplastic |
| PID | proportional integral derivative; a control scheme |
| PMSM | permanent magnet synchronous motor |
| RBT | rotary breaker test |
| RPM | revolutions per minute |
| s | roller gap separation |
| SHBT | split Hopkinson bar test |
| SMC | SAG mill comminution test |
| $t_{10}$ | fraction of breakage products less than 1/10th of original particle size |
| $t_n$ | fraction of breakage products less than 1/n of original particle size |
| UFLC | ultra-fast load cell device |
| USB | universal serial bus |
| VFD | variable frequency drive |
| $\mu$ | coefficient of friction |

# 1 INTRODUCTION

From the earliest history, mining has been one of the cornerstones of human civilization. When we look at the development of cultures, we tend to define and view them according to the minerals and materials they were using. As the societies progressed and grew, tools and implements were introduced to better exploit the available resources. The first evidence of mining by humans date back to 450,000 B.C.E. with the Stone Age man breaking rocks by hand to produce tools. Fire setting was being used to break rock around 5,000 B.C.E. in Egypt, followed by the discovery of smelting copper and the beginnings of the Bronze Age. The first recorded use of explosives happened in 1627 around a mountainous area of Joachimsthal in the Czech Republic. Finally, the invention of dynamite in 1867 enabled modern large-scale mining operations. A modern mine site may produce 500,000 tons of excavated material in a single day. (Spitz and Trudinger 2019, pp. 2–4) The growing demand for minerals and the unprecedented scale of operation create new challenges for the mining industry. Greater volumes of materials need to be produced from lower grades of ore, transported from more remote locations, from greater depths, and processed at lower costs.

One of the key processes involved in minerals extraction is *comminution*. Comminution refers to the processing step where mineral ores are broken down to smaller particles in order to liberate the materials of interest. Insufficient comminution results in poor mineral liberation, whereas breaking the particles too fine leads to excessive energy consumption, poor selectivity and low recovery in the subsequent separation processes. Crushing rocks to pieces can be responsible for over a quarter of the total energy consumption of the mining industry (Tromans 2008) so mapping the properties of the rock materials in a mine is important for optimizing the design and use of the crushing and grinding equipment. If comminution or breakage tests are needed for improving the economics of mining, so the comminution tests themselves need to be economical and effective to employ.

A new prototype device was commissioned as a part of a project to develop a fast, low-cost and reliable breakage characterization test for geo-metallurgical modelling. The design and construction of the prototype were the responsibility of the author of this thesis. The main body of the work was conducted during the spring and summer of 2019 under the work package one of the Geomet Rolls Breakage Test (GRBT) project. The work was done in collaboration between the Oulu Mining School and the Mechatronics

and Machine Diagnostics research group of the Intelligent Machines and Systems unit in the University of Oulu. The testing of the prototype was done in collaboration with Tabatha Chavez Matus in part to provide material for her thesis. The basic specification and requirements for the device were provided by Dr. Marcos de Paiva Bueno and refined as the work progressed.

The aim of this thesis is to proof the concept of the new instrumented crusher for measuring the comminution characteristics of rock particles. It includes a short literature review to explore comparable comminution testing devices and their uses, some information about the relevant properties of rock materials for the design of the prototype, and a look into the basic value of mechatronic systems with relevant examples in the context of the prototype. More detailed information about the prototype itself is provided through the chapters on development, manufacturing, and testing the device. Finally, some analysis and discussion are presented about the issues and potentials for improvements discovered during the work.

# 2 LITERATURE REVIEW

Commonly used comminution tests may be categorized broadly into three groups. The first group of rock mechanical tests are characterized by very gradual and slow application of forces on samples of rock to the point of breakage. The second group of particle breakage tests employ dynamic impact forces to break the sample. The third group of grindability tests measure the attrition of materials inside a rotating mill with or without grinding media. The comminution behaviors of rock materials vary with the amount, type, and rate of stresses being generated by the testing equipment, as well as the dimensions and shapes of the particles. Different tests and methods may be used for different applications to reflect the actual minerals processing context for the industry, and the same test methods may be applied at different scales - from early evaluations with single particles to pilot scale plant testing with hundreds or thousands of kilograms of sample material. (Mwanga et al. 2015) Small scale comminution testing generally involves sample sizes between 5 - 300 kg (Chandramohan et al. 2015). This chapter explores the second group of comminution tests followed by a review on the relevant properties of the materials being tested, and a general overview into mechatronic systems with examples in the context of the prototype device.

## 2.1 Impact type breakage tests

A selection of impact type tests found in the literature includes the Drop Weight Test (DWT), the SAG Mill Comminution test (SMC), the Ultra-fast Load Cell Device (UFLC), the Twin Pendulum test, the Split Hopkinson Bar test (SHBT), and the Rotary Breaker Test (RBT) (Mwanga et al. 2015). In addition to these commonly used tests and devices, various instrumented versions of the actual crushing equipment themselves can be used (Refahi et al. 2010; Lieberwirth et al. 2017).

### 2.1.1 Drop Weight Test

A drop weight test device illustrated in picture 1. consists of a weight falling onto a hard anvil with the sample being tested placed in between. For smaller particles, the anvil may be replaced by a die that holds the particle in place. The weight is typically guided down by means of linear rails or rods. The velocity and energy of the impact can be varied by changing the lifting height and mass of the drop weight. (Mwanga et al. 2015)

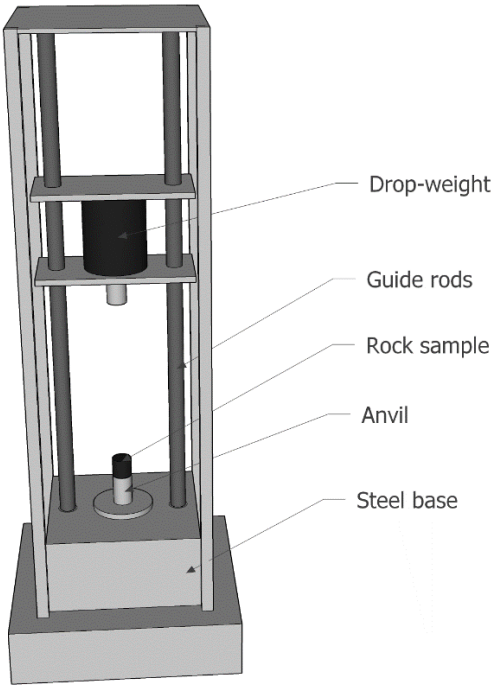


Picture 1. The Drop Weight Test device.

The intent of the test is to measure the comminution of the sample in relation to the energy input, typically expressed in kilowatt-hours per ton. As the resulting rock fragments are sifted, the percentage of finer fragments $t_n$ passing through *1/n* the size of the original particle can be related to this specific energy by the mathematical function presented in equation (1). The parameters *A* and *b* are empirical parameters obtained by fitting the mathematical model to a specific ore at different specific energy levels. The energy level *E* is varied to produce the data for this fitting. (Mwanga et al. 2015)

$$t_n = A(1 - e^{-bE}) \tag{1}$$

The obtained values can then be used for predicting the comminution energy consumption for process modeling. A size fraction of 1/10 is commonly used for characterizing ore samples. The value $t_{10}$ can be related to different fractions $t_n$ by performing the test on multiple different particle sizes at multiple different specific energy levels. This procedure requires 15 repeats of the test and approximately 75–100 kg of material to be tested. An abbreviated version of the test known as the SMC or SAG Mill Comminution test reduces the number of trials by using a single particle size fraction. This provides parameters *A* and *b*, but not the different $t_n$ curves. (Mwanga et al. 2015) The abbreviated test may be used for estimating variations within an ore body that has already been

characterized by the full Drop Weight Test (McKen and Williams 2005). Another variant of the drop weight test known as the UFLC, or Ultra-Fast Load Cell device, employs an instrumented anvil consisting of a steel bar with strain gauges for measuring the impact force. The drop weight itself may be instrumented in a similar fashion, and the displacements and forces measured from the device are used to estimate the actual energy absorbed by the tested particle. Knowing the principle of work as equivalent to force over distance, the energy absorbed by the particle may be computed using integral calculus. (Mwanga et al. 2015) An obvious feature of the drop weight test is that the particles and their breakage products can remain on the anvil under the falling weight, so some breakage products may be re-broken into finer pieces while others may escape. This may cause variations in the apparent energy efficiency of the test and influence the results.

### 2.1.2 Twin Pendulum

The Twin Pendulum Test works similarly to the Drop Weight Test by using two opposing hammers as shown in picture 2. The hammers are released to strike simultaneously on a sample particle held up on a pedestal. In the Bond Twin Pendulum Test, the hammers are incrementally lifted and released from higher deflection angles until the particle breaks. In any version of the test, the potential energy of the hammers is used to determine a crushing work index in kilowatt-hours per ton. (Mwanga et al. 2015)

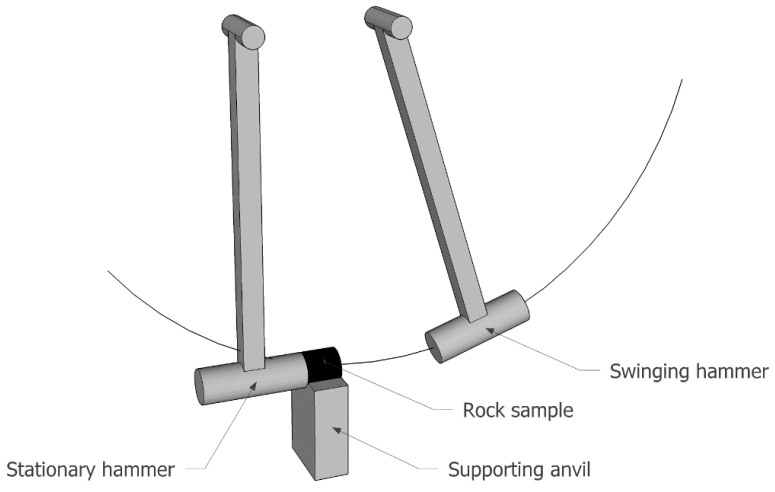


Picture 2. The Twin Pendulum.

As with the drop weight test, instrumented versions of the twin pendulum test exist. The swinging hammers can be fitted with sensors to record their precise motions. The actual energy consumed by breaking the particle can be recorded by leaving one hammer stationary against the sample particle and swinging the other hammer. The remaining energy in the system causes the first hammer to swing upwards on impact. The amount of energy transmitted through the particle can then be measured by the rebound movements of the two hammers. (Mwanga et al. 2015)

### 2.1.3 Split Hopkinson Pressure Bar

The Split Hopkinson Pressure Bar was originally developed to test the propagation of stresses in materials, mimicking the stress waves produced by the detonation of explosives. The basic structure of the device shown in picture 3. consists of two steel bars that are aligned on bearing blocks that permit the axial movement of the bars. The sample particle is held in close contact between the ends of the two bars while a heavy projectile is propelled to strike the end of one bar by the means of a pressurized gas gun. The two bars holding the sample are instrumented with strain gauges to measure the strain wave passing through the system and reflecting inside the steel bars. The amount of energy absorbed into the rock particle is calculated from the impact energy of the heavy projectile and the strain waves measured from the steel bars as the energy transmits from one bar to the other. (Mwanga et al. 2015)

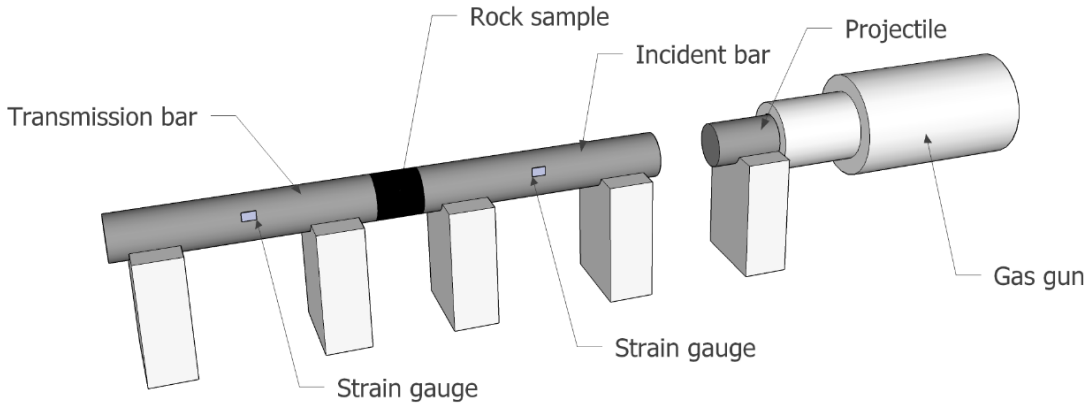


Picture 3. The Split Hopkinson Pressure Bar.

### 2.1.4 Rotary Breaker

The Rotary Breaker is based on the principle of single impact testing, where a particle is accelerated to strike an instrumented surface to record the resulting forces. This is accomplished by a centrifugal rotor in the middle of the device, that throws the sample particles out of the feed channel against a stationary ring around the rotor. The basic structure of the device can be seen in picture 4. A sawtooth profile on the inside of the stationary ring allows the particles to strike in a perpendicular direction to the surface. The continuously turning rotor allows the insertion of particles through the center and the device can measure particles in rapid succession. (Mwanga et al. 2015) Possible sources of error come from early breakage by the particle bouncing inside the rotor as it is being accelerated, and from any uncertainty over the particle's speed as it exits the rotor.

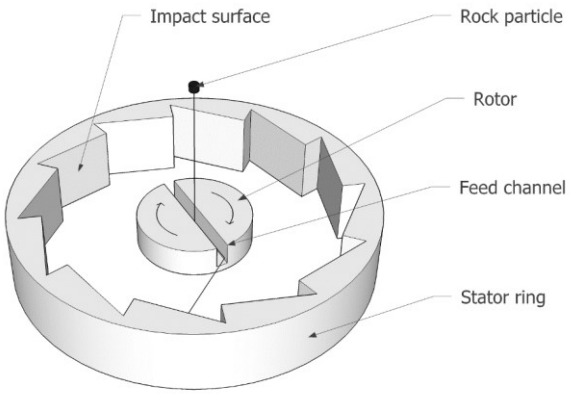


Picture 4. The Rotary Breaker.

### 2.1.5 Instrumented crushers

One example of an instrumented crusher is the Double Roll Crusher in the technical center of the Institute of Mineral Processing Machines of the TU Bergakademie Freiberg. A drawing of the crusher can be seen in picture 5. The machine consists of two smooth rollers inside an adjustable split frame. The long rods used for holding the frame halves together are instrumented with strain gauges to measure the forces that push the rollers apart during particle breakage. This way the crusher can measure the forces that result from passing material between the rollers. When the driving motors are powered off and the rollers are left to spin under their own inertia, the amount of energy consumed by particles passing through the rollers causes the speed of the rolls to drop. This may be used to measure the amount of energy that is consumed while crushing the particles. This

device has been used to study the forces present in the crushing equipment itself more so than the properties of the particles being crushed. (Lieberwirth et al. 2017)

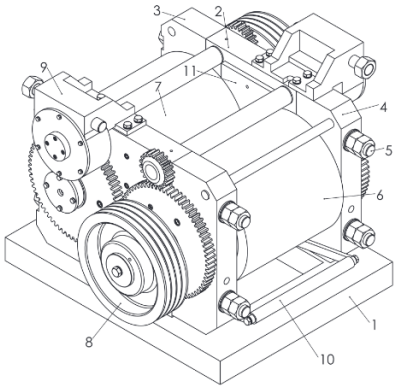


Picture 5. The Double Roll Crusher (Lieberwirth et al. 2017).

Another example is a device for measuring the grindability of coal for use in thermal power stations. The patent drawing can be seen in picture 6. This double roll crushing device consists of a fixed roller and a movable roller hinged around a pivot on the end of an L-shaped lever. The other end of the arm is pressing against a load cell, which in turn is fixed to the rigid base of the machine. The load cell measures the forces that are transmitted from the crusher gap through the pivot and into the frame of the machine while lumps of coal are passed through the rollers. (Noguchi and Watanabe 1992)

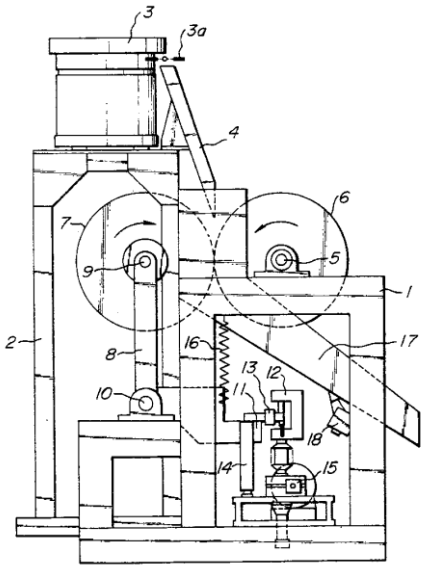


Picture 6. Apparatus for measuring grindability of powder material (Noguchi and Watanabe 1992).

Yet another variant of the machine extends the L-shaped lever into a U-shaped bracket as seen in picture 7. The force exerted on the roller bends the structure and the ends of the bracket move closer together. A transducer - a variable transformer as mentioned in the patent - measures the distance to a very high precision. The beam acts as a spring so the amount of deflection of the roller can be used to measure the force that is being applied to the roller. This device was designed for testing the strength of abrasive grains such as industrial diamonds, so the rollers were proposed to be made of very hard materials, for example tungsten carbide. (Morris W.G. 1994) These two devices do not directly measure the energy of comminution – only the forces involved.

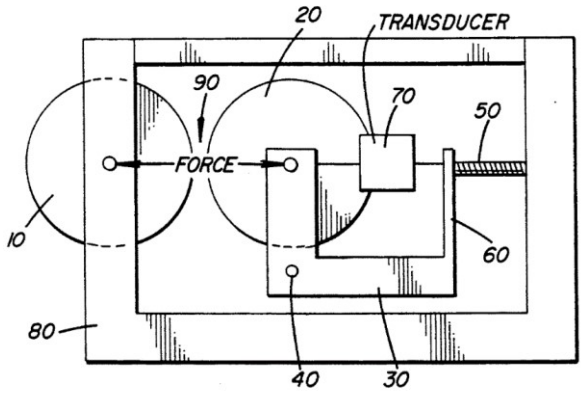


Picture 7. Device for measuring the strength of abrasive grains (Morris W.G. 1994).

## 2.2 Properties of rock materials

It is known that the dynamic fracture strength of a rock material is highly dependent on strain rate (Mwanga et al. 2015; Zhang 2004; Grady and Lipkin 1980). Various measured or quoted values for the fracturing stress of various rock types under different conditions can be found in the literature. A sampling of such values is listed in table 1. This listing does not differentiate between tensile and compressive stress.

Table 1. Amount of stress to fracture rock.

| |
|---|
| 10–125 MPa (Grady and Lipkin 1980) |
| 3–60 MPa (Zhang 2004) |
| 7.5–110 MPa (Yan et al. 2011) |
| 5.6–142 MPa (Whittles et al. 2006) |
| 6.62–60.22 MPa (Liu and Xu 2013) |

Very high strain rates as produced by a Split Hopkinson Pressure Bar can produce peak stresses in the range of 170–280 MPa at fracture (Liu and Xu 2013). For very low strain rates. a wider range of values between 5.7–464 MPa under uniaxial compression and 0.5–30.5 MPa in tension can be found. The corresponding surface hardness for the softest and hardest rock materials range between 9–100 in Shore hardness units. (Altindag and Guney 2010)

The main reasons for the low energy efficiency of comminution processes are in the way the crushing and grinding equipment work, by applying randomly distributed forces on the particles. This results in energy losses through friction, elastic deformation, kinetic losses, et. cetera. It is possible to derive a theoretical upper limit to the energy efficiency of comminution. With certain assumptions and approximations, the ideal limiting efficiency of breaking a spherical rock particle can be calculated to fall somewhere between 5–10 % (Legendre and Zevenhoven 2014). Crushing a particle more rapidly to apply a higher loading or strain rate causes more energy to be absorbed, which causes more branching fractures, secondary cracking, and micro-cracking. This leads to more of the rock being broken down to finer particles. At the same time, the non-absorbed energy is consumed in the kinetic energy of the resulting breakage products (Zhang et al. 2000).

In a study done on marble and gabbro rocks, using a Split Hopkinson Pressure Bar, the energy required to split a drill core sample was found to increase rapidly with the loading rate. The samples were made of 33 mm diameter drill core, cut into lengths of 40 mm and prepared with a notch, leaving approximately two thirds of the lengthwise cross-section area intact. The energy absorbed in splitting the drill cores was found to range between 0.604–7.336 Joules, while the impact energy into the system was varied between 6.3–141.0 Joules. The corresponding efficiency of energy absorption was found to be in the range of 5–14 %. (Zhang et al. 2000)

In another case, the comminution energy of granite and limestone samples were tested and modeled using a laboratory scale jaw crusher. A Discrete Element Method computer model of the same device was used for comparison. The specific comminution energy for a single 6-centimeter spherical granite specimen was found experimentally to be 1696 kJ/ton. The matching computer model gave a result of 1702 kJ/ton. With a good agreement between the model and the experimental data, the computer model indicated 410 Joules of energy absorbed by the particle. (Refahi et al. 2010)

A plausible energy requirement for the prototype device can be estimated by these values. Impact energies of up to 141 Joules may be required at high strain rates (Zhang et al. 2000). If we assume the energy consumption to be proportional to the volume of the material being crushed, we may use the ratio of volumes to extrapolate for different particle sizes. Using this method, the example of the jaw crusher would indicate an energy demand of 51 Joules for a 30 mm sphere. A cylinder of 33 mm by 40 mm would require 102 Joules, and a 50 mm spherical particle would require 237 Joules of energy to break.

## 2.3 Mechatronic systems

A breakage testing device can be a purely mechanical system, such as the Twin Pendulum or the Drop Weight Test in their simplest forms, where the device is neither powered nor instrumented in a direct sense. These tests rely on the mechanical action of a falling mass with a known energy, and the resulting breakage products are carried away to be measured elsewhere. When the test is made more elaborate, instrumentation is added. Typically, a strain gauge signals the stretching or compression of a piece of metal and a data recorder is used to capture the amount. In the case of the Split Hopkinson Pressure Bar, optical gates may be used to measure the velocity of the projectile before impact to know its energy. (Mwanga et al. 2015) The device can be powered and instrumented, but the operation and interpretation of the results remains a manual task that depends on the fine skill and experience of the researcher or technician whose job it is to use the device. The devices may be electromechanical in the sense that they incorporate motors, actuators, sensors and electrical circuitry, but this does not necessarily make them mechatronic devices or systems (Hsu 1997).

A mechatronic system in its abstract is deceptively simple. It picks up signals and processes them to generate some action or force as its output. What makes it different from conventional mechanisms is that it reacts to the signals in a suitable way (Acar and Parkin 1996; Hsu 1997). This is to say, the mechatronic device is not just turned on or off by a signal, or directly commanded by the signal to do something, but it is rather self-adjusting to it. The device might for example ask the operator how much force they wish to apply and then independently decide on the appropriate actions to achieve it. Broadly speaking, a mechatronic device is a hybrid of electrical and mechanical functions that complement each other in an intelligent way (Acar and Parkin 1996; Hsu. 1997). When the basic testing device is elaborated further into a system to include powered drive

mechanisms with feedback control, as well as automatic data gathering and interpretation, the device no longer functions as a simple mechanical tool to be used by the technician but an intelligent appliance that works for them. The mechatronics engineer's job is to integrate the electrical, the mechanical, and the computational technology into such systems (Cetinkunt 2007).

### 2.3.1 Power and control

Many types of machinery are powered with electric motors. In the past, electric motors were controlled manually or designed for certain operating characteristics, whereas modern control electronics and power semiconductors permit all types of electric machines to operate under automated control. The three basic types of motors – DC, induction, and synchronous – can all be used for variable speed operation. (Sen 1990)

The simplest option of the three is the DC or Direct Current motor. A mechanical switch called the commutator is responsible for changing the direction of the input current to alternate inside the motor in time with its rotation, so the controller of the motor needs only to adjust the applied voltage or current to change the speed and torque. The DC motor is nearly ideal from a control perspective, but it suffers from mechanical wear and reliability issues because of the sliding contact switches inside the commutator. The induction motor and the synchronous motor are much better in terms of reliability and cost since they do not operate by mechanical switching, but for the same reason they can't operate on direct current. The controller must apply AC or Alternating Current, varying the frequency, voltage and current to drive them. This is more complicated and often more expensive because it requires a frequency converter known as a Variable Frequency Drive or VFD. To remedy these issues, a type of synchronous motor called the Permanent Magnet Synchronous Motor (PMSM), in some configurations known as the Brushless DC motor (BLDC), was evolved by integrating the AC drive electronics with the motor. This type of motor incorporates an absolute position sensor to measure the angle of the rotor in order to commutate the current electronically. It behaves very much like the DC motor for any external control circuitry. Since the commutation circuitry is electronic, it may be implemented with digital or analog control schemes that include intelligent features such as internal speed or torque regulation, current regulation, or self-tuning adaptive algorithms for responding to different load conditions. (Sen 1990) Since a brushless DC motor can be made programmable, it may even perform automated motion

sequences and respond to external events independently. Though often abstracted away as just another motor, a BLDC motor is really a mechatronic system of itself.

A typical control block diagram of a Brushless DC motor presented in picture 8. contains a microprocessor, a transistor driver to amplify the control signals, six power transistors to commutate the currents, and three motor coils. In the example illustration, the microprocessor is identified as a Microchip PIC microcontroller, but any suitable part may be used. The inputs to the microprocessor can include control messages and signals, or the processor may simply run the motor as fast as possible with the power supplied for it to mimic a traditional DC motor. The idea of the motor operation is to switch currents through the stationary motor coils A, B and C in a sequence that forms a rotating magnetic field. Since the rotating part of the motor contains a permanent magnet, it aligns with the field and synchronizes to the rotation. The rotating part is named the rotor, while the fixed part of the motor is known as the stator. The motor coils made of insulated metal wire are often called phases, in reference to their order or phase in the switching sequence. The phase coils are wound around posts or slots in the stator.

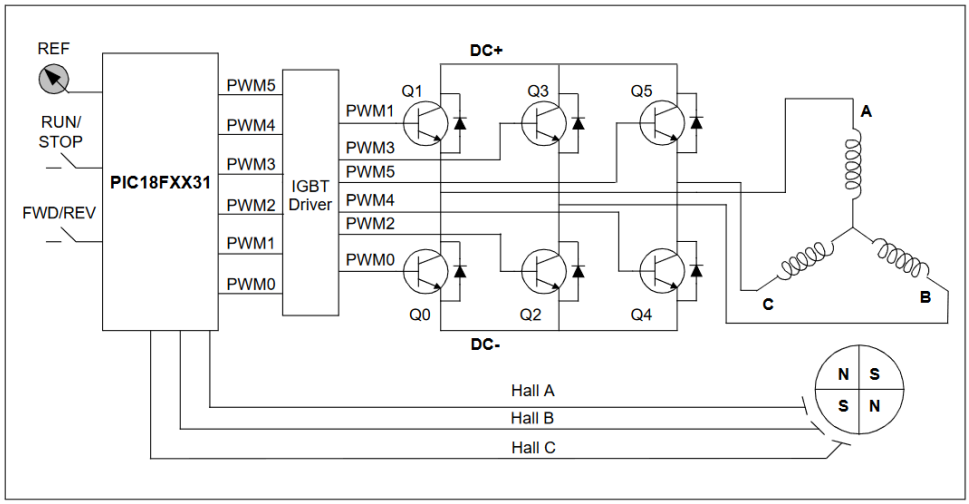


Picture 8. Brushless motor control block diagram (Yedamale 2003).

An actual motor may divide the phase coils around the stator perimeter into multiple windings. They form moving electromagnetic poles that circle around the stator over the commutation switching sequence, always in multiples of two since the sum of their fields cannot physically have an odd number of poles. The permanently magnetic rotor too has at least one pole-pair. In the minimum configuration of two stator poles and a rotor with one permanent pole-pair, one full electrical rotation of the switching sequence produces

one full rotation of the motor. When a synchronous motor is built with more than two poles, the number of electrical cycles per mechanical rotations multiplies by the number of rotor pole-pairs. (Yedamale 2003) This improves the torque characteristics of the motor at the expense of speed.

Below the motor coils in the diagram, the circle representing the rotating permanent magnet is sided with the absolute position sensors which provide feedback to the microprocessor. The electronic path from the spinning rotor to the controller and out to the stator coils through the transistor power switches forms a closed control loop that is characteristic of mechatronic systems. This enables the motor to react and respond to varying load conditions in a controlled manner - as opposed to an open control scheme without feedback. The controller can switch at a set frequency without the feedback from the absolute position sensors, so the system can operate as a regular synchronous motor at a precise speed, but this method requires accelerating the motor very slowly to avoid a loss of synchrony (Sen 1990). Open-loop control is mostly suitable for loads that are predictable or synchronize easily to the driving cycle, while closed loop control is better with dynamic loads and accelerations that may exceed the torque capabilities of the motor. A programmable controller may switch between the two as needed.

One way to implement the absolute position sensors is to observe that a permanent magnet motor is also a generator and produces a voltage waveform when a rotor magnet pole passes over a phase winding. Any two of the three phases can be powered while the controller measures the third for the generated voltage. This “sensor-less” configuration simplifies the construction but works poorly at low speeds because the generated voltage is proportional to the speed of the rotor. The motor must start under open-loop control before it can sense its own rotation (Yedamale 2003). This is unsuitable for loads that require significant torque from a standstill.

The commonly used sensor type for a brushless motor is the Hall effect sensor. It is a type of magnetic sensor that can measure the polarity and magnitude of a magnetic field by its effects on a small electric current flowing inside a semiconductor. Since the effect is very weak, a Hall sensor typically incorporates a sensing amplifier and signal conditioning in the same device. The output may be conditioned to produce an on-off signal, or a voltage, or a current proportional to the direction and magnitude of the field. (Honeywell 2019; Yedamale 2003) In a motor application, a simple digital on-off signal is used to detect the

rotor magnets passing over the sensor. A block diagram of such a sensor is presented in picture 9.

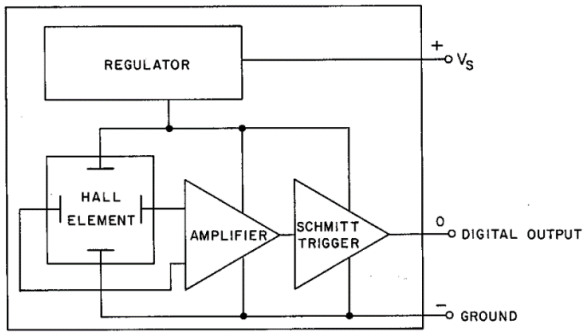


Picture 9. A digital Hall effect sensor block diagram (Honeywell 2019).

Three Hall sensors are typically placed evenly between the stator windings at 120 electrical degrees apart. In a two-pole motor this means 120 physical degrees. Correct Hall sensor placement is crucial for the efficient operation of the motor. The optimal placement around the circumference of the motor is just 7.5 electrical degrees wide. This divides into physical degrees according to the number of poles around the motor. (Tsotoulidis and Safacas 2014)

To understand what the microprocessor in the motor controller does, a diagram of the internal organization of a commercial brushless motor controller is shown in picture 10. This particular controller has multiple functions involving position, velocity, electrical current, and their corresponding feedback paths from internal and external sensors. The controller can be programmed to use any of these features. In current controlled mode, the motor current is set to select the torque produced by the motor. In velocity mode, the controller itself changes the torque to maintain the set velocity. In the position mode, the controller adjusts the velocity, with or without an acceleration ramp, to turn the motor a set amount. The controller is also programmable to handle logic inputs, analog voltage signals, and digital commands from other computer systems, using a rudimentary programming language to assemble code that can be stored in the controller. The program can respond to limit switches, user input from buttons, or other external sensor inputs and perform automated motion sequences. (Trinamic 2016) Such elaborate controls are not necessarily used: for a motor that is designed simply to spin, the Hall sensors may signal the next commutation step directly without any computations made in between. Therefore, a simple logic circuit may take the place of the microprocessor and the

manufacturer saves the time and cost of programming it. This is typical of small motors such as those in computer cooling fans.

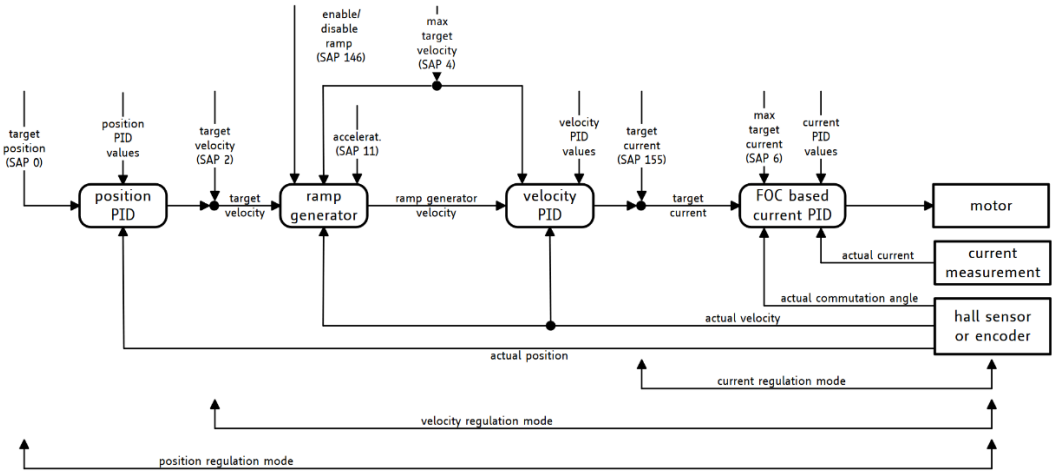


Picture 10. Cascaded regulation diagram (Trinamic 2016).

A recurring element in the schema is the PID block, which stands for a Proportional-Integral-Derivative control element. A simple block diagram of a PID element can be seen in picture 11. This is a commonly used method for responding to the feedback information using basic differential and integral calculus. A PID-controller computes the difference between an input signal and a measured feedback signal to quantify the deviation between the input of a desired state and the achieved state of the system as measured by the sensors. This difference is used as an indicator of the present error of the system, to count an accumulation of the error to represent the past state of the system, and to predict the development of the error to account for a future state of the system. The combination of the past, present and future error quantities is then used to generate a control signal output to drive the system to where it should be. (Cetinkunt 2007, p. 64)

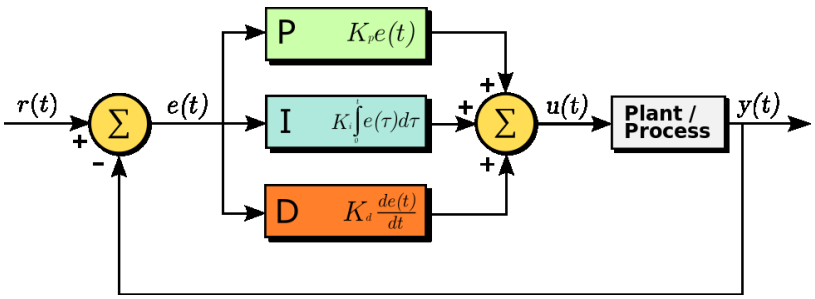


Picture 11. PID control elements (Urquizo 2011).

Starting from the left of the diagram, the measured state of the system $y$ is subtracted from the input or the requested state $r$ to produce the error quantity $e$. The error quantity is then inserted to the three PID elements. In the Proportional element, the error is multiplied by a constant $K_p$ to create a control signal according to the present error value. In the Integral element, the error signal is integrated over a time period $T$ and the result is multiplied with a constant $K_i$ to create a control signal by the past error of the system. The Derivative element likewise calculates the difference of the error signal over time and multiplies the result by the constant $K_d$ to make a control signal about the predicted future state of the system. Finally, all these elements are summed together to a single control output signal $u$ which is sent to the process or device that is being controlled.

Variations and additions to this basic scheme are possible and the elements can be paired or cascaded one after another to form any combination of P, I and D elements. This is done to shape the transient and static response of the controller. For example, the controller can be formed as a cascade of PD and PI pairs where one is responsible for transient errors and the other deals with steady-state errors. This way the two can be adjusted separately without affecting each other. All the combinations are fundamentally based on selecting the constants $K_{p,i,d}$ to tune the response of the whole control element to the system being controlled. (Cetinkunt 2007, pp. 65–74) In the case of the motor controller, the internal organization of the PID block is usually fixed by the manufacturer, leaving only the selection of the constant coefficients, possibly the integration time $T$, and some other factors such as how often the evaluation is computed. The tuning of these parameters is often done by hand, but it may also be solved mathematically or with machine learning algorithms. In more advanced cases, a separate program algorithm may observe the system and continuously adapt the tuning parameters to minimize the error of the PID-controller in real time.

There are many more finer points to the design, construction and control of a brushless DC motor, but understanding these basic factors gives a good starting point for practical application and understanding of the motor as a mechatronic system.

### 2.3.2 Sensors and signal capture

A mechatronic system or device needs sensors to collect information for control feedback and monitoring purposes. The output of the sensors and acquisition of data can also be the desired result of the operation of the device. In many cases an actual sensor, such as the Hall sensor in the electric motor, comes built with all the elements needed to translate a physical variable into an intelligible electrical signal. Not all sensors are complete like this, and the signals they produce may need further interpretation to be useful for the application. A basic understanding of sensors and the process of capturing the signals produced by sensors is necessary to make effective use of them.

The fundamental function of a sensor is to translate or *transduce* the measured physical variable into a change in some electrically measurable property of the sensor itself. This basic concept of a sensor can be seen in picture 12. Some sensors change in resistance, inductance, or capacitance, while others may produce electrical signals in the form of current or voltage in response to the physical variable they are measuring. (Cetinkunt 2007, p. 217) An example of the former is a variable resistor or a rotating potentiometer, which by itself does not produce any signals until measured electrically. An example of the latter could be the microphone of an electric guitar, which produces a weak current induced by the guitar string moving in a magnetic field. In either case, the change in property and the signal produced is often very small or weak and the sensor is easily disturbed by any electrical load placed on it. (pp. 220–222) Since any device that is receiving the signal is necessarily an electrical load on the sensor, the signal needs to be amplified to a practical level before it can be processed. In this context, the processor does not necessarily mean a digital computer – it may be any electrical circuit or device, such as an analog filter circuit or an indicator dial.

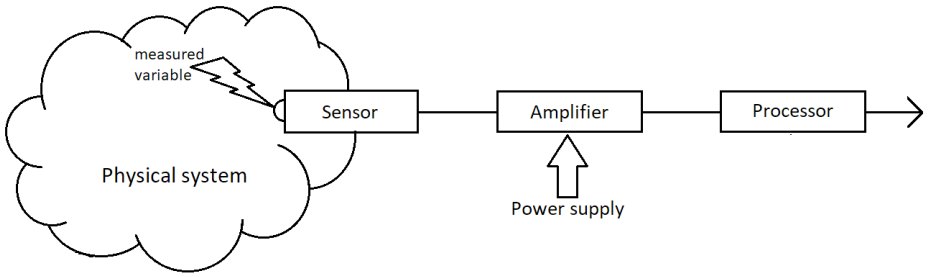


Picture 12. The components of a sensor: sensor or transducer, amplifier, processor.

A real sensor is never entirely accurate to the physical quantity it is trying to measure, and it's always subject to some amount of error from noise and variations in the sensor and the environment. Other errors may be introduced by fluctuations in the power supplied to the sensing amplifier, or along the signal paths between the components. This limits the smallest difference the sensor can detect, otherwise known as the sensor's *resolution*. The sensor is also limited in its dynamic response by the slowness of its reaction to the physical event. This limits the *bandwidth* of the sensor, which is the greatest frequency of events the sensor can measure without too much error. For accurate dynamic measurements, a sensor should have a bandwidth of at least ten times the maximum frequency of any signal component being measured. Errors and biases will also occur due to non-linearities in the transducer and amplifier, and because of physical tolerances in manufacturing the individual parts. Sensors generally need to be calibrated or characterized to interpret their signals precisely. (pp. 218–219) It may also be noted that some sensors have a minimum frequency they can detect due to the way they transduce a physical effect into an electrical signal. An electromagnetic coil, as in the earlier example of the brushless electric motor, cannot produce a detectable voltage if the magnetic field it is measuring is changing too slowly. Equally, if the magnetic field is changing too rapidly, the inductance of the coil will impede its effect and the signal is suppressed again. The bandwidth of a sensor is more generally the band or range of frequencies it can detect. Distortion of the measurement will happen when approaching either end of that range. A sensor also has some characteristic *frequency response* as a result of its physical and electrical properties or design. It may emphasize some signal frequencies while suppressing others within its bandwidth.

Bandwidth and resolution are also important in another sense when dealing with digital signal capturing. A sensor is only as good as the system that measures it, and vice versa, so the properties of the signal capture and recording system should be chosen accordingly. This task is made easier with the choice of a digital sensor which already includes a built-in analog-to-digital converter that turns the continuously variable output of a transducer into discrete digital values. Recording the output of an analog sensor with a digital computer however becomes a matter of *sampling* the signal in discrete units. Unlike the sensor which is limited by its physical qualities, the resolution and bandwidth of a digital system can be chosen more freely by selecting data acquisition hardware with a suitable *sample rate* and *sample resolution*. Better equipment of course comes at a greater price.

The sample rate can be related to the bandwidth by the theory on communications developed by Nyquist and Shannon. The Nyquist limit of a sampling system is the highest frequency that can be represented by the recorded data and therefore the upper limit of its bandwidth. If the sample rate of the data acquisition system is at least twice the highest frequency in the signal, the recorded signal can be reconstructed perfectly from the data to the accuracy of the sample resolution. (Landau 1967) The sample resolution refers to the number of possible discrete values or levels in each sample, which is usually expressed by the number of digital bits of information per sample. The product of the sample rate and the sample resolution results in a *data rate* expressed in bits per second. The data rate is also called "bandwidth" in other contexts and should not be confused with the signal bandwidth of the sensor and data acquisition system.

To understand what this means in practice, we can use an example of a simple data acquisition method that can be used with almost any personal computer. If the signal can be amplified and conditioned into a waveform with a maximum amplitude of approximately 1 Volts, it can be recorded digitally as a sound file with the computer's sound card. The signal processing and analysis may then be performed with any suitable program, such as MATLAB®. (Chandra and Ismail 2009) With the knowledge that crushing a rock between two rollers takes on the order of tens of milliseconds, we might decide that the shortest event we are interested in recording takes one millisecond. The reciprocal of this event time period corresponds to a frequency of one kilohertz. Since the recommendation for accurate dynamic measurements is to have a bandwidth at least ten times the frequency of interest, the sampling system should have at least 10 kHz of bandwidth. A common computer sound card can be set to record at a standard sampling rate of 22.05 kHz giving it a bandwidth and an upper frequency of approximately 11 kHz. If the sample resolution is set at 16 bits per sample, the data rate becomes roughly 176 kilobits per second. The data rate may be important in determining the amount of processing power, memory or network capacity required from the computer system.

A regular sound card however isn't necessarily linear in its frequency response, and it is liable to have other distortions and biases because it is not built for exact measurements. The actual performance of an analog-to-digital converter can rarely reach the accuracy indicated by the number of bits used for the conversion. This is because of the random errors added to the signal by the converter itself. The transmission of the signal through the device is subject to noise and the actual information carrying capacity of any such

communications channel diminishes in proportion to a logarithm of the ratio of random noise in the signal (Shannon 1949). When the converter's resolution is increased to the point where the smallest difference it can measure becomes less than the level of noise, the additional bits of resolution no longer improve the accuracy of the result because the information is masked by the noise. Trying to measure smaller differences in the signal simply by sampling at a high resolution requires that multiple subsequent samples are averaged together to diminish the amount of uncorrelated noise in the result. This has the same effect as reducing the sampling rate, which is why the nominal resolution of a typical cheap analog-to-digital converter can actually be achieved only at the expense of its bandwidth.

For a point of reference, the NI 9237 strain gauge bridge module contains a power supply, a signal amplifier and a high-resolution analog-to-digital converter for measuring resistive transducers. A graph of the frequency response of the module over the operating bandwidth can be seen in picture 13. The *gain* measured in decibels notes the attenuation or amplification of the signal. The sharp drop of the input gain is produced by an internal filter which removes signal frequencies close to and over the Nyquist limit of the output sample rate. This is done to remove the badly distorted out-of-bandwidth, otherwise known as *aliased* signals from interfering with the results. This module *over-samples* the input with 64 times the rate of the output to average the results for better accuracy. At the full output sample rate, the internal sampling rate of the module is 3.2 MHz while the output is 50 kHz at a resolution of 24 bits. (National Instruments 2019a) This device is designed for high accuracy dynamic measurements of very small signals.

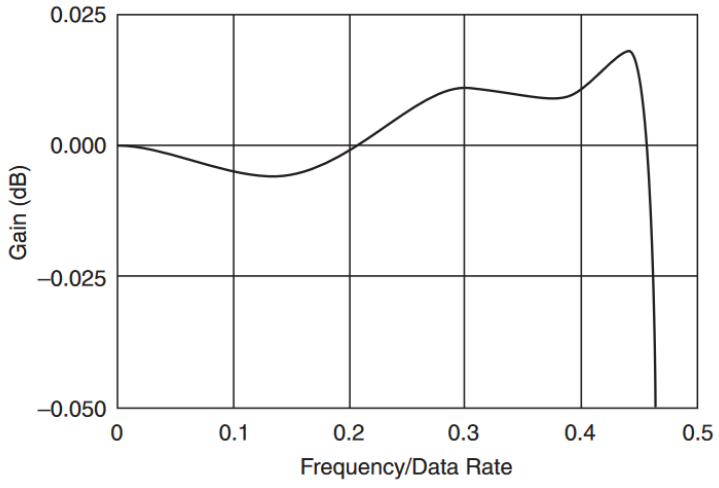


Picture 13. Frequency response of the NI 9237 module (National Instruments 2019a).

The choice of a sampling frequency and sample resolution depends on the type of the signal produced by the sensor and how that information is used. Consider the case of an encoder that produces a series of discrete pulses in response to motion. Such an encoder could measure the rotation of a wheel, so that the rate of the pulses corresponds to the rate of rotation. In this case it is not important to measure the level of the pulse, so the sample resolution can be as low as one bit. In fact, no analog-to-digital conversion needs to take place at all if the signal is already a series of countable pulses. The timing of signal transitions from one state to the other contains all the information (Cetinkunt 2007, pp. 247–248). If the sampling rate is fixed at 10 kHz, each sample period takes 0.1 milliseconds. If the encoder is producing 100 pulses per second, once every 10 milliseconds, the relative error of measurement is the smallest measurable difference or the ratio of the sample period to the signal period: 0.1 ms divided by 10 ms. This quantization error places the result within 1 % of the actual pulse period. Another way of looking at the matter is to note that a smallest measurable difference of 1 % represents slightly less than 7 bits of information because a binary number of 7 bits can represent a quantity in $2^7 = 128$ parts.

Counter-intuitively, if the encoder was made better by increasing the number of pulses per revolution, the accuracy of the measurement would get worse because each pulse would be shorter relative to the fixed sample period. In that case, it could be better to use a different method for processing the signal. The device could count the number of pulses over a longer time period or average the measurements of subsequent pulses together instead of measuring each individual one. Other mathematical methods and algorithms may also be used. A Discrete Fourier Transform computes the spectrum of different frequency components in a record of measured samples. The frequency distribution may then be interpolated to find the strongest peak corresponding to the pulse frequency. If there is enough time to collect at least 1024 data points containing at least 20 cycles of the waveform, the relative error can be brought down to less than 0.04 %. (Jain et al. 1979)

The implementation of the signal capture and data acquisition system depends on the application and nature of the sensor and the signal being measured. It is by no means restricted to digital sampling with computers either although digital systems are by far the most common today. It is up to the designer to choose the applicable means and methods.

# 3 DEVELOPMENT AND MANUFACTURING

The purpose of the prototype was to design, build, and test the feasibility of a low-cost, fast and reliable device for breakage characterization on a laboratory scale. Since the equipment is a scaled down version of a type of crushing machine already used in the industry, many of the same issues and questions encountered in designing industrial comminution equipment apply to the design of the prototype device as well. This chapter details the design and construction process from the initial specifications to the finished device.

## 3.1 Basic specifications

The structure of the new device was proposed as a variation of an instrumented roll crusher with an adjustable gap. The device should operate in a continuous fashion, with the potential for automating the operating procedure in later designs. The running speed of the rolls should be adjustable for the overall energy level, rate and synchronization of the device. For a basic operating procedure at a low level of automation, the operator of the device would:

1. prepare a batch of approximately 30 particles
2. adjust the running speed and gap size for the desired energy level
3. feed the machine with the particles one by one
4. collect the product from a bin underneath the rolls

The device should be able to process the 30 particles in rapid succession while measuring the energy consumption of comminution and the breakage force of each individual particle. The applied energy level would be chosen as the size reduction ratio of the crusher by varying the gap size relative to the size of the particles. The potential particle sizes to be tested with the device range between 16 - 50 mm and the main interest are particles in the range of 20-30 mm with a maximum reduction ratio of 4:1. This means the device should be adjustable for a gap separation between 4-50 mm or more. The device should supply at least 100 Joules of energy to the particle with a design target up to 250 Joules as estimated from the values found in the literature. (Refahi et al. 2010; Zhang et al. 2000)

The device should also incorporate safety features by the European Union Machinery Directive. For a proof of concept and prototype device as a laboratory experiment, no specific safety features are required (European Union 2006). Reasonable safeguards for the protection of life and limb should be provided in any case. The user should be adequately shielded against flying debris and from the unintentional insertion of body parts into the moving mechanism. A relief mechanism should be incorporated to protect the device against damage from extremely hard rock types or unintended hard objects.

## 3.2 Mechanical requirements

For design purposes, it is not strictly necessary to find exact values for the ultimate fracture strength of various rock types. A plausibly high value can be chosen to represent the properties of a typical hard rock that might be tested. Since the machine cannot be designed to handle infinite amounts of energy or force, a cut-off point should be chosen, and the excess can be handled by the relief mechanism. An estimated dynamic strength of 100 MPa was chosen to represent a typical hard rock. Assuming a spherical particle with a diameter of 30 mm, the primary breakage surface across the particle was approximated as 700 $mm^2$. Following the simple relation of stress as force over area, the peak force should reach 70 kN. No part of the machine should show more than 0.1 % strain under this maximum load to make sure the deformation of the structure remains small, linear and reversible.

The crushing event of a single particle in a double roll crusher takes on the order of 20–35 milliseconds (Lieberwirth et al. 2017). Assuming 200 Joules of energy is spent in 20 milliseconds, a peak power demand of 10,000 Watts can be expected. Since the device is not required to process a contiguous back-to-back feed of particles, the device can spend some time to speed up between measurements. If one particle is crushed every five seconds, the average power demand of the device becomes 40 Watts.

If the particle is too large compared to the rollers, the resultant force pushing the particle out of the roller gap becomes larger than the force of friction pulling the particle in. The particle slips and may begin to bounce between the rollers. The diameter of the rollers depends on the friction between the roller and the particle. The maximum equivalent feed particle size $d$ can be calculated in relation to the roller diameter $D_W$, the gap separation $s$, and the coefficient of friction $\mu$, by the following formula: (Lieberwirth et al. 2017)

$$d < (D_W + s)\sqrt{1 + \mu^2} - D_W \quad (2)$$

Choosing a medium value for the coefficient of friction at μ = 0.24 from values found in the literature (Lieberwirth et al. 2017), the formula can be approximated as:

$$d < 1.028\,(D_W + s) - D_W \quad (3)$$

Re-arranging the formula for $D_W$ gives:

$$D_W > \frac{1}{7}(250d - 257s) \quad (4)$$

This simplification makes it possible to calculate a suitable roller size for each particle and gap opening. Given the requirement of 4:1 reduction and a particle size between 20–30 mm, the roller diameter becomes 530–796 mm. Choosing a reduction ratio of 3:1 produces a roller diameter in the range of 470–704 mm. Large particles and high reduction ratios would require impractically large rollers to ensure that the particle is grabbed every time. A compromise on the choice of roller diameter was agreed at 600 mm. Roller surface speeds up to 3.0 m/s may be employed. This means the drive system should reach speeds up to 95 revolutions per minute. Higher speeds may result in worse nipping behavior due to reduced friction. The coefficient of friction becomes smaller if the particle's falling speed differs from the roller surface speed so the particle drop height will depend on the speed of the rollers. (Lieberwirth et al. 2017)

## 3.3 Design iteration

With the specifications and requirements in place, the initial design step was to explore the problem space for different approaches. Since the intent of the device was to measure the force and energy of crushing a particle between two smooth rollers, any device which mimics this action could do the same duty. The CAD and Finite Element modeling work were done using Autodesk Inventor Professional 2019.

The starting point was to use regular store-bought bicycle hubs and rims with hardened steel hoops fixed around the rim. Placing two such wheels in-line would emulate a narrow part of a larger double roll crusher. If a 70 kg rider is supported by a single bicycle wheel, and the dynamic load is estimated to reach ten times this static loading, the maximum

loads such wheels should be expected to carry come on the order of 7 kN. This is just 10 % of the load specification. The bicycle wheel design could have unreasonably large amounts of flex and yield against the load. A hub-less design with only a steel hoop supported around the inside by heavy-duty bearings was also considered, but this was deemed difficult to manufacture, and with either design the metal hoop could easily run out of shape form repeated impacts.

The next idea involved a heavy pin rolling over a level surface. The crushing gap would be adjusted by support rails that lift the pin above the surface. The question of sample insertion and product removal was raised. It was noted that the material feed would be best operated by gravity, therefore the crushing surfaces needed to be vertical. This led to the idea of using two sectors of a larger diameter wheel moving in synchrony. To reduce the size of the device even further, only one sector is necessary while the opposing surface can consist of a flat surface moving along a pair of vertical rails. A force sensing element could be built into the surface.

To further reduce the number of moving parts, the pivoting wheel sector could be guided to rock against the stationary crushing surface, supported by bearings on both ends. The development of the idea can be seen in picture 14. In the final form, the device would resemble a jaw crusher with a constant gap separation. The reciprocating motion of the rounded jaw would crush any particles dropped between the opening, and the resulting fragments would fall through the gap to a collection tray below.

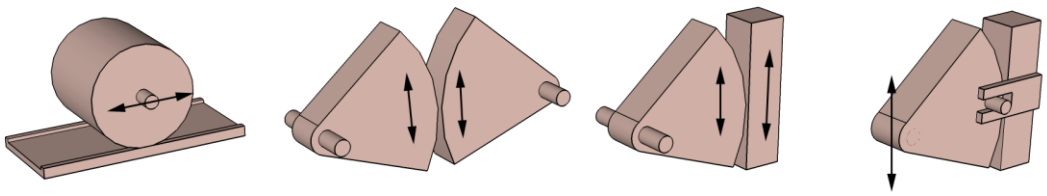

Picture 14. Four crusher concepts from rolling to rocking.

Further analysis on the proposed construction revealed several issues. The device would have to operate at relatively low speeds to avoid vibrations, and the drive mechanism would have to deal with very high torque and high accelerations to supply the necessary crushing forces. A large flywheel to drive the mechanism would have to be provided

anyways to store the required amount of energy. Criticism was raised by Prof. Dr.ing Holger Lieberwirth over the structural rigidity and mechanical soundness of the construction since the driving power into the mechanism would have to be transmitted through and against multiple bearings and linkages. The device would have to be made with unreasonably tight tolerances and closely fitting parts, since any looseness in the mechanism would produce shocks and vibrations that would interfere with the sensors and measurements. The measurement of energy consumption during the varying accelerations of the parts of the mechanism would be difficult. The idea of a reciprocating mechanism was abandoned.

The concept was taken back to the original bicycle wheel. After weighing the possibilities, it was deemed feasible to manufacture the wheels from solid steel with the equipment in the university machine workshop. With the solid wheels themselves working as flywheels to store energy, the drive system could be made much simpler. The use of energy could then be accurately measured by the loss of rotation of the wheels. The wheels would need to be sized correctly to store enough energy without adding too much rotating mass, in order to maximize the resulting difference in speed and ensuring particle breakage. The construction of the wheels would depend on the constraints specified in the initial requirements. The shape and form of the rest of the device was then designed around the two-wheel concept. A 3D model of the designed structure can be seen in picture 15 and an illustration of the wheel as finally designed can be seen in picture 16. with more information about the design choices presented later under the section for parts.

An alternative design to the straight and narrow wheel was also discovered. If small diameter cylinders were made with their ends beveled, facing each other end-to-end at the angle of the bevel much like a pair of bevel gears, the gap between the bevels would approximate the nipping behavior of larger diameter straight rollers. The smaller the angle of the bevel, the greater the effect becomes. A particle would enter between the ends of the rollers where they are separated and get pulled a half or a quarter turn around the bevels into the gap. The smaller diameter would result in lower surface speeds, so the rollers could be spun faster to achieve the same flywheel energy capacity with less mass. The disadvantage of this setup is the centrifugal force that may throw the particle out of the gap before it gets completely broken. The idea was considered interesting, but not suitable for this prototype.

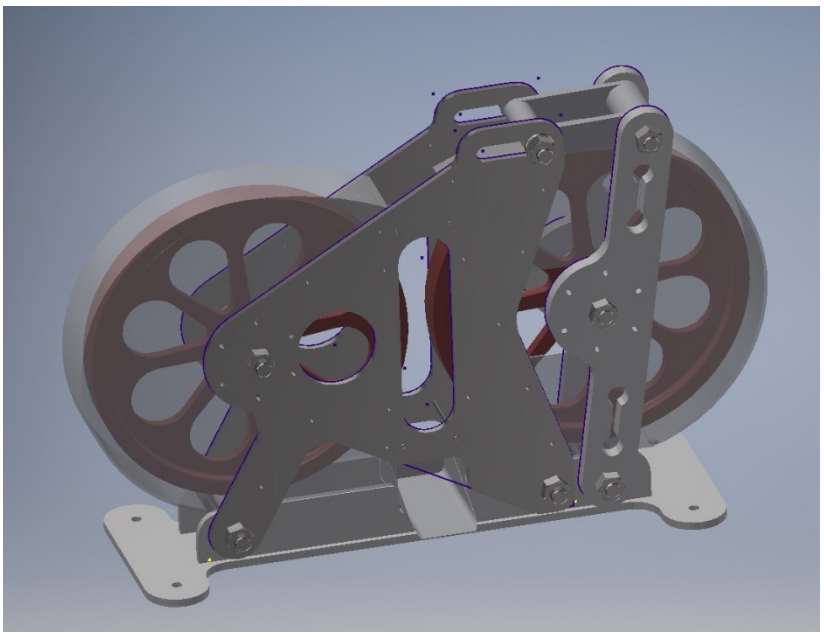

Picture 15. A CAD model of the double wheel crusher.

## 3.4 Parts

The actual mechanical construction of the crusher was split into three logical units with interfaces to the others: the wheels, the power or drive system, and the frame. The choice of the interfaces would then define the mechanical construction. A fundamental design choice was made to have the wheel axle fixed to the frame instead of to the wheel – to act as a cross-member of the frame structure for the rigidity of the entire device. A non-rotating central shaft meant that the drive system would need to interface with the wheel hub or rim, and the choice for the power transmission method would determine the interface with and define the structure of the frame.

### 3.4.1 Wheels

With the wheel diameter fixed at 600 mm and the maximum particle size defined at 50 mm the choice was made to manufacture the wheels out of steel plate with a nominal thickness of 60 mm. Very hard materials in excess of 800 HB would be needed to deal with all the possible types of rocks that could be tested, but using such hard steels would risk chipping the wheel itself. High hardness in steel is a compromise with brittleness and low impact resistance. For an example, the impact resistance of Domex 700MC steel can fall below 80 J/cm$^2$ in a Charpy V-notch test at room temperature, while a softer Hardox 400 steel can withstand impacts up to 170 Joules per square centimeter (Mazur and

Mikova 2016). The material choice is a compromise between hardness to resist abrasion and pitting from impacts by the rock particles, toughness to resist fracturing and chipping the steel, and machineability with the equipment at hand. The choice was made to use a wear resistant Raex® 450 steel with a hardness value between 420–500 HB, a yield strength of 1200 MPa, and an impact resistance of 30 J/cm$^2$ at -40 °C (SSAB 2019). This material is similar to the Hardox 400 steel and was readily available from a local supplier.

The design of the wheel began by approximating the amount of rotating mass needed for the desired amount of energy. Since the overall dimensions of the wheel were already defined, material was removed from the center and sides of the wheel, leaving enough to withstand the specified load with minimum distortion. A worst-case stress under 150 MPa with the nominal load placed on the edge of the wheel was deemed acceptable. The result of the load simulation can be seen in picture 16. Without much material property data for the steel, this estimate at least limits the amount of strain in the material well under 0.1 % and limits the stress far enough below the yield point that no permanent deformation can be expected to occur. The finished wheel can be seen in picture 18.

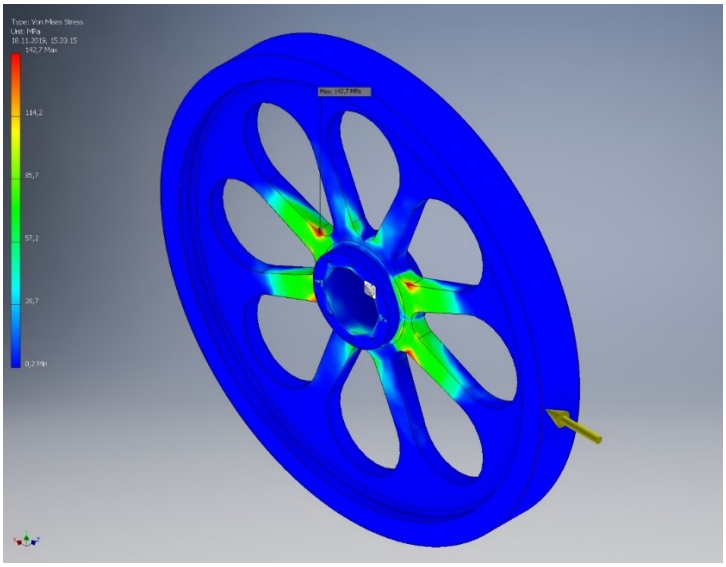

Picture 16. Wheel Finite Element model under maximum loading.

The steel was ordered pre-cut into circular blanks, which were then rough-cut on a water jet cutter to remove much of the excess material. The wheels were then cut on a lathe to finish the outer surface and center bore in one attachment to ensure alignment. The choice was made not to turn the sides of the wheels on the lathe, as these features would be non-critical and take a very long time to cut. Instead, the relief cuts on the sides were made on

the shop's Mitsui Seiki HR5B horizontal mill. There were some difficulties with mounting and aligning the wheels to the milling cutter. This was due to the machine being old and out of adjustment. This was expected and compensated for by adding balancing weights to the wheels. The bushings and shafts for the wheel were turned on a lathe out of common mild steel.

The bearing components were designed to fit inside the wheel. A hollow shaft would provide the seat for two bearings with two closely fitting bushings sliding over the shaft from both ends to hold them against a central ridge. A threaded rod through the shaft would tighten the whole unit between the frame plates. This would allow the frame of the machine to be made of simple plates without special pillow blocks for external bearings. The bearings would be held inside the wheel center bore with two circular end plates. The initial design also incorporated two rubber V-rings under the end plates, but these had to be omitted from the actual construction. The intent of the rubber V-rings was to provide a light centering force for the bearings as well as shield them from dust. A cutout view of the wheel bearings can be seen in picture 17.

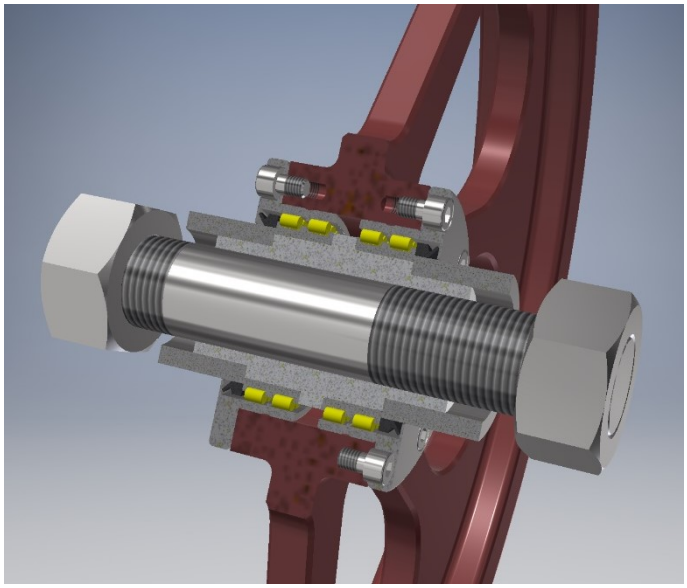

Picture 17. Roller bearings inside the wheel hub.

The choice of bearings was done with the help of the SKF bearing election guide. The sizing of rolling bearings at low speeds and high impact loads should be done according to the static load rating $C_0$. A static safety factor between 3...4 may be chosen to permit some pitting or deformation of the bearing elements. A minimum load of 1–2 % of the dynamic load rating C is also recommended to ensure that the rolling elements do not

drag and slide inside the bearing. Using a greater safety factor would ensure no impact damage to the bearings, but it would require oversized bearings and put the minimum loading well below the recommended value. (SKF 2019) Two suitable roller bearings of the type NNCL 4912 and NA 4912 were found. Their properties can be seen in table 2.

Table 2. Load ratings of two bearings (SKF 2019a, 2019b, 2019c).

| Bearing | $C_0$ | C | Static safety factor for 70 kN / 2 |
|---|---|---|---|
| NNCL 4912 CV | 137 kN | 78.1 kN | 3.91 |
| NA 4912 | 114 kN | 60.5 kN | 3.26 |

The two bearings are identical in their major dimensions, but not in internal details. The design was initially made with the NNCL 4912 CV bearing, but the item was not available for order, so the second bearing was substituted. A design error was made in assuming that the bearings were largely identical, and that the CAD model of the bearing was fully representative of the real item, so the V-ring seal was placed against a flange which on one bearing was on the inner ring, and in the other on the outer ring. This made it impossible to put the seal inside the hub. The rings were instead pressed against the hub from the outside. While this would work, the friction caused by the rubber V-rings was found to vary and the sealing was not very effective, so they were taken out entirely. This would leave the bearings somewhat unshielded from airborne dust, but this was acceptable for a proof-of-concept device. The bearing end shields were simply made with a small enough opening around the central shaft to keep the bearing components from sliding out. It was found that the motor chosen to drive the wheel would provide enough axial force to center the wheel on its bearings if the device sits on a level floor.

The wheel mass without the bearing components came to be approximately 48 kilograms and the full wheel assembly was a little over 52 kilograms. This was found to be very heavy to handle, but still manageable by a single person. Assembly by hand without lifting aids was found possible, but not recommended for the risk of injury. The amount of imbalance was found to be no more than 200 grams at the inside rim of the wheel. The wheels were finished with a coat of red corrosion resistant paint and the balancing weights were fixed over the wheel spokes with strong epoxy glue. The moment of inertia with the balancing weights, motor and bearing components in place was estimated from the CAD

model and calculated to be 2.916 kg-m$^2$. The model was varied slightly to test for a range of possible deviations in the actual manufactured wheel and the uncertainty of the value was estimated at less than 3 %. The wheel would store approximately 57 Joules of energy at 60 RPM and 129 Joules at 90 RPM. With both wheels in motion this sums up to 114 and 258 Joules respectively.

### 3.4.2 Power transmission

The first consideration was to drive the wheels by a sprocket, or a pulley attached onto the wheel hub end plate. A small DC or AC motor would provide the driving torque through a chain or a belt at some suitable reduction ratio. Alternatively, a small rubber wheel could be attached to the electric motor and pressed against the outer surface of the crushing wheel to drive the wheel by friction. The latter arrangement would provide the benefit of completely disconnecting the drive during measurements with no energy lost to back-drive the mechanism. Finally, a direct drive option was discovered with a motor for a washing machine. With this motor option, a ring of magnets fixed onto the crusher wheel would produce the driving torque against a matching set of electromagnets fixed to the frame with no mechanical contact between the two. Engaging and disengaging the drive torque could be done electronically without the need to separate parts of the machinery. LG brand direct drive motors as seen in picture 18. were bought from a spare parts supplier and modified to fit the crusher wheels.

Picture 18. A washing machine motor installed on the finished crusher wheel.

Modifications to the motor involved cutting out the center of the magnet retaining plate to fit it around the wheel hub. Holes were drilled for carriage bolts to secure the plate against the wheel spokes. Mounting holes for the stator part of the motor were provided in the machine frame, and bolts with nylon-insert lock nuts were used to adjust the distance between the stator and the frame. Since the motor has the property to pull the magnetic rotor towards the iron of the stator, the motor tends to center itself axially. This feature allows the motor to act as a magnetic bearing for the wheels and keeps the bearings from drifting to the sides and dragging internally.

The construction of the washing machine motor is a variation of a brushless DC motor (BLDC). In this case, the motor was constructed with three electrical phases of 12 magnetic coils in series with the phases connected in a star or wye configuration. Measuring the series resistance over two phases produced a value of approximately 8 Ohms. Since the intention was to drive this motor designed for a 240 Volt appliance with a safer 24 Volts DC, this resistance would limit the input current of the motor too much and result in very low efficiency. A simple benchtop stand was constructed to hold the motor halves and allow the rotor to turn. A current draw not much over 1 Amperes was measured and the motor could be stalled easily by hand. The motor windings were modified to split each of the phases into two parallel strings of six coils. The resulting connection was measured at approximately 4 Ohms across two phases and the current was limited at 3.5 Amperes by the motor controller, providing a maximum of 84 Watts to the motor.

The current draw and torque of a BLDC motor is greatest at stall and reduces linearly with speed until the generated voltage of the motor matches the driving voltage. The theoretical maximum speed is reached when the current and torque diminish to zero. (Yedamale 2003) It follows that the maximum output power is attained at half the maximum speed and therefore at half the stall current. This simplification means that the current at maximum power output for this motor would be 3 Amperes and the input power at 24 Volts would be 72 Watts. The Joule heating in the resistance of the windings at 3 Amperes consumes 36 Watts. The highest speed measured on the benchtop test was measured at little over 121 RPM as reported by the motor controller, so the peak output power was estimated as 36 Watts at 60 RPM. The two motors and wheels should reach a combined flywheel energy level of 100 Joules in under two seconds, and 250 Joules in approximately five seconds assuming negligible losses to friction.

The motor controller chosen for the task was the Trinamic TMCM-1640 with 100 Watts of continuous output power capacity at the maximum rated voltage. The controller features current sensing and limiting, the option of using one of the motor windings as a sensing element for commutation switching, as well as support for magnetic Hall-sensors or encoders for measuring the motor angle and speed. The controller supports remote control by USB or a serial interface, and it can be programmed to operate independently using a proprietary programming language. The controller also provides an analog input for voltage signals and a pair of switches or buttons. (Trinamic 2019) The controllers were programmed to adjust their speed according to an analog voltage signal which would be provided by a simple wired hand controller. This was done to control the motors directly without relying on any software running on a computer. The controller includes an external connection terminal to interface with a computer or other control system, but the hand controller will always override the external signal when the switch is turned to the “Off” position. A diagram of the speed selection circuit can be seen in picture 19. In this circuit, the potentiometer on the left selects the average speed for the two motors, and the potentiometer on the right divides the signal value between the two outputs A and B for adjusting the balance. An example listing of the motor controller program can be found in appendix 1.

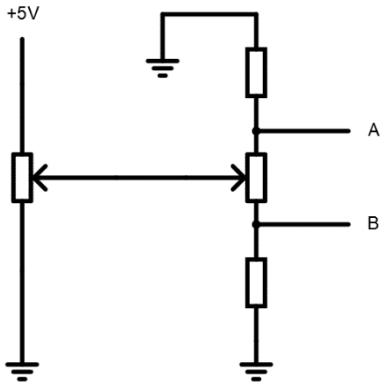


Picture 19. Speed selection circuitry.

The washing machine motor included a magnetic quadrature sensor, but this was found to be electrically incompatible with the Trinamic controller. Three generic Hall sensor components identified by a type code "C1024 Hall-effect switch" were installed to each motor to construct a conventional Hall sensor block. The components were mounted onto

a sheet of acrylic in place of the original speed. A circuit shown in picture 20. was used to measure and display the Hall sensors signal on an oscilloscope. The signal shows a steady triangular waveform when the sensors are aligned.

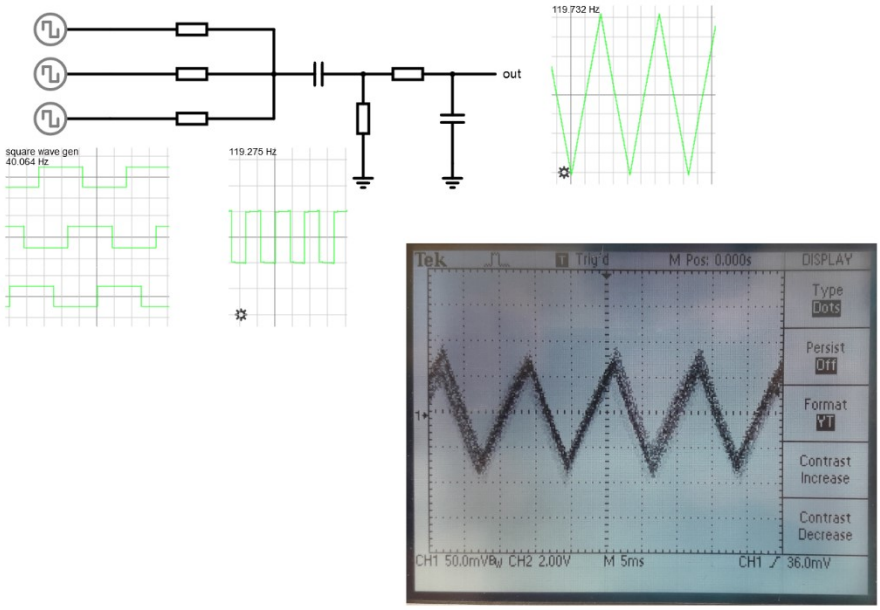


Picture 20. Hall sensor measurement circuit and oscilloscope trace of the signal.

The motors were initially powered by a laboratory power supply unit. When the device was assembled, a dedicated 24 Volt 12 Ampere DC switch mode power supply unit was used instead. After reaching the requested speed, the motors would tend to brake and produce switching transients which triggered an over-voltage protection fault in the power supply. This shut down the unit every time. Large electrolytic capacitors and reverse current blocking diodes were added between the power supply unit and the motor controllers to stop this failure from occurring.

### 3.4.3 Frame

The frame of the device was designed to be made of steel plates with minimal machining and welding. All the frame plates were cut to their final dimensions on a water jet cutter, including all the mounting holes for the various parts of the machine. This method produces no heat effects on the steel and no thermal expansion of the material being cut. The disadvantage is the relative inaccuracy due to spreading and skewing of the jet especially in thicker materials. This was taken into account by designing the features with

wide enough tolerances to fit. Still, some holes had to be touched with a file to pass a bolt through because the cutter had left a protrusion on the edge.

The frame consists first of a bottom plate with two upright plates welded on along its length. On one end of the upright plates, a cylindrical bushing extends through both sides to provide the lower hinge for the load beams. The hinge bushing is welded to the uprights. Two more attachment points are provided with simple holes next to the hinge and at the other end of the bottom frame. Shorter bushings between the upright plates cover the threaded rods that clamp the frame sides to the bottom frame. The frame sides consist of simple cut plates with holes for attachment to the bottom frame, for mounting the wheel hubs, the motor, plastic covers and other accessories. The frame sides area cut with access and viewing ports to the crusher gap and motor area, and a slot in the upper part of the side plates for the gap adjustment mechanism.

The load beam consists of two long plates with holes at both ends and middle. These plates are held apart by bushings that work as hinges at the ends, and by the wheel in the middle. Cut openings along the middle of the plates on both ends produce thinner sections along the edges of the beam where the stress and strain from the bending of the beam become concentrated. The bending of the beam acts as a spring element against the crushing forces, and the amount of deflection and force can be measured by strain gauges placed on the thinned sections of the beam. This turns the load beam into a structural sensor element.

Two short and narrow pieces of plate steel were welded between two bushings to construct a link arm between the upper end of the load beam and the upper slot of the frame plates. The whole construction is held together with threaded rod and nuts tightening the plates and beams against the bushings between the frame. Thin sheet metal shims were rolled around the threaded rods to align the center shafts of the wheels to their mounting holes in the frame. Sleeve bearings were inserted around the bushings at the load beam hinges. A general view of the frame and the wheels while they are being test fitted can be seen in picture 21.


Picture 21. The frame and wheels being tested for fit.

The frame parts were made of common S355 structural steel plate and similar grades of steel in bar stock for bushings. 30 mm plate was used for the load beams while the rest of the frame uses 15 mm plate. The frame is essentially held together by friction. The M30 size threaded rods and nuts are tightened to permit no slipping between the parts under normal operation. This construction provides a relief mechanism that gives under extreme loading and allows the frame to come apart for maintenance. The joint between the link arm and the upper frame is adjustable along the slot cut into the frame, and the operator of the machine can adjust the holding force by tightening this joint. The link arm can be moved in excess of 100 millimeters along the slot. This adjusts the gap between the wheels by half the amount, giving a useful adjustment range from 0 to 50 millimeters. A simple scale is glued to the edge of the frame plate to read the gap separation and a pointer on the link arm indicates the amount.

Load simulations on the frame and wheels with a 70 kN center impact force indicate that the gap between the wheels may grow by 0.5 millimeters with the passing of a very hard rock particle. Most of the displacement happens by the bending of the load beam. With the load offset 10 millimeters from the edge of the wheel, the wheels begin to flex at the spokes and the gap grows by 0.77 millimeters at the loaded side. The wheel tends to get deflected sideways by approximately a millimeter. The effect of loading can be seen

exaggerated in picture 22. The loading on the frame stays below 150 MPa and no greater forces can act on the device as long as the relief mechanism is properly adjusted. The operator may over-tighten the adjustment link but doing so with normal hand tools requires physical strength and effort.

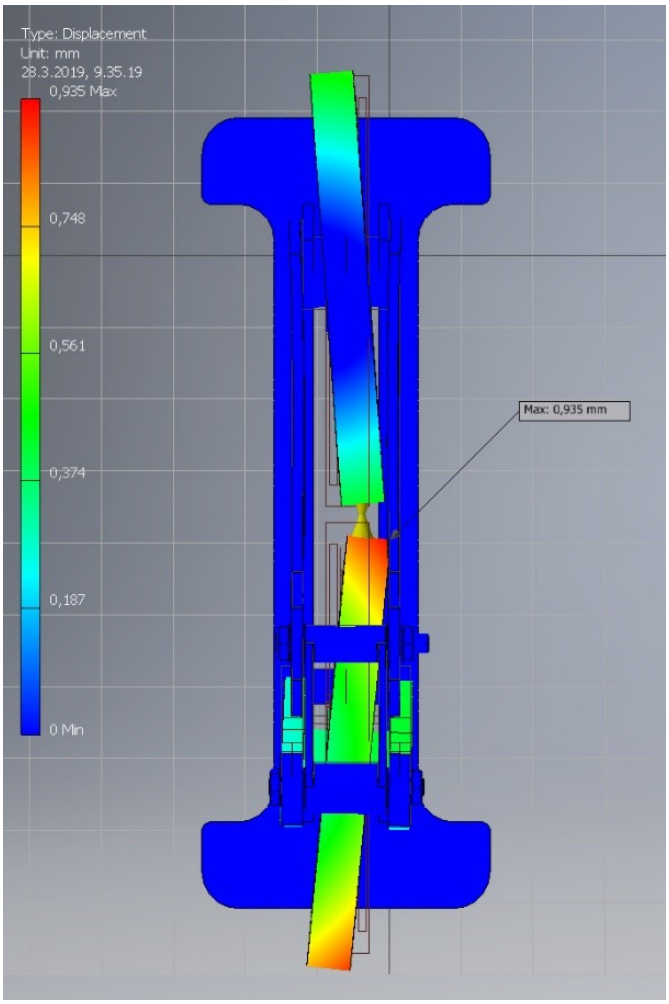


Picture 22. Deflection of the wheels under load increased for visualization.

The fully assembled device shown in picture 23. includes shields made of impact resistant clear PETG plastic and metal fenders covering the top part of the wheels. The gap between the wheels is enclosed on two sides by plastic guide fences with small hinged doors added to permit the removal of stuck rock fragments from the gap. The fenders were cut from thin galvanized sheet steel on a water jet cutter and bent into shape by hand. The plastic shields and fences were cut from 5 mm sheet on a 75-Watt laser cutter in the university Fab Lab fabrication laboratory. Various other parts such as mounting brackets and a shelf for the product collection tray were fabricated out of 0.5 mm sheet steel with a manual bending brake and metal shears.

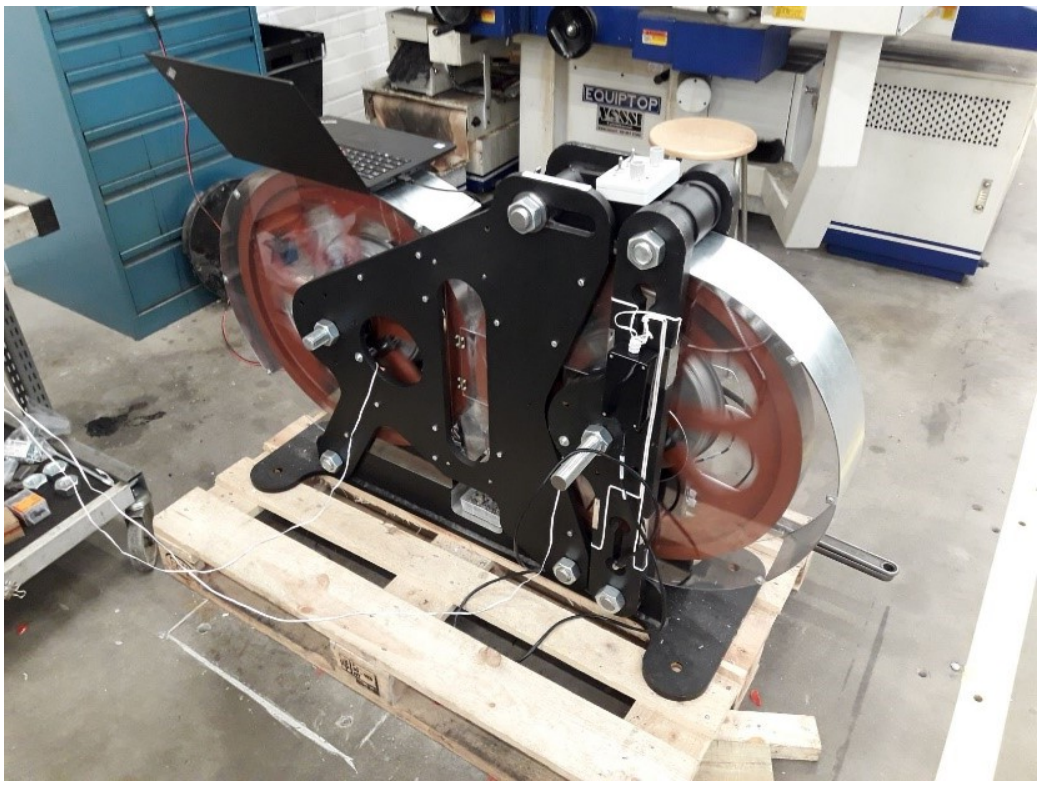


Picture 23. Fully assembled device during motor testing.

## 3.5 Sensors and measurements

The method of capturing signals and processing them in a manner that produces meaningful results for the operator is equally important, even when the information is not used directly for feedback into the operation of the device itself at this stage in development. In the prototype device, the operator is still responsible for control adjustments. The device follows the set parameters and reports to the user when it has reached them.

### 3.5.1 Data acquisition hardware

A decision was made to use a purpose built analog-to-digital converter module specifically designed for strain gauge measurements. A National Instruments NI 9237 four channel strain gauge bridge module with a maximum sampling rate of 50 kHz and a resolution of 24 bits was chosen to for the task (National Instruments 2019a). This module, and other supporting hardware, were lent by the university Mechatronics and Machine Diagnostics research unit for testing and development purposes. The strain gauge module was connected to a laptop computer via a cDAQ-9171 CompactDAQ

chassis, which operates over a standard USB 2.0 interface (National Instruments 2019b). Four NI 9949 screw terminal adapters with four RJ-50 cables were used to connect the strain gauge bridges to the input module. The terminal adapters provide direct electrical contacts to the input module (National Instruments 2019c). Identical hardware was bought from National Instruments after the system was proven to work.

The strain gauges were connected in a full bridge configuration, using one input channel for each side of the load beam. With two of the four input channels still available, ordinary resistors were used to construct dummy load cells with fixed values and the speed signals from the two wheels were summed to these resistor bridges. This way, all the measurements could be made synchronously with the same input device, which means that the software running on the laptop computer does not need to correlate inputs from different sources in real time. The real-time processing requirements are all delegated to the input module.

### 3.5.2 Optical encoders

The original intent was to connect the signal from the motor Hall sensor block to the data acquisition hardware to record the speed of the wheels directly from the motors. Trying to measure the wheel speed over a short time period would produce wildly varying results. At first this appeared to be a problem with the motor control and tuning program. Some time was spent in trying to run the motor at a fixed frequency without feedback from the Hall sensors in the attempt to force the motor to revolve steadily, but this failed consistently. On closer examination, the individual variations in the magnets and the periodic change in the motor air gap were found to modulate the signal enough to interfere with the measurement. The actual wheel speed could not vary greatly from one revolution to the next, but the measurement would be useful only as an average over a full revolution.

As a solution, an optical encoder wheel as show in picture 24. was manufactured to fit over the other end of the wheel hub. The encoder wheel was cut on the Fab Lab 75-Watt Epilog laser cutter out of thin plywood and glued in place with a supporting plastic ring. A simple TCST1103 infrared gate was mounted onto the frame with the encoder wheel running between the gate. Power to the infrared diode was taken out of the National Instruments strain gauge module and the resulting signal was wired to a resistor bridge connected to the input channel. A circuit diagram of the solution can be seen in picture 25. Care was taken not to exceed the supply power limits of the strain gauge module. This

configuration improved the measurement greatly and proved that there was nothing wrong with the motor control program. The speed signal from the Hall sensors was fine enough for controlling the motor.

Picture 24. Optical encoder ring installed on the wheel hub.

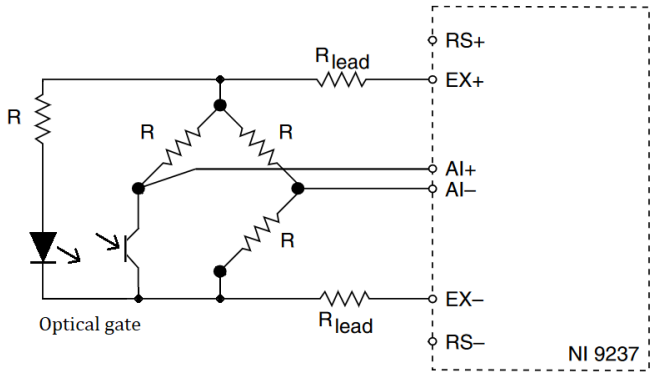


Picture 25. Optical gate circuit implemented as a resistor bridge.

A very finely toothed encoder wheel might have been used for better resolution, but it would have been prone to breaking. With 128 teeth in the encoder, the angular resolution between two edges is approximately 1.4 degrees - but this cannot be relied on. The teeth are never perfectly cut and evenly spaced. Instead, the measurement software should count multiple teeth on the wheel and calculates the average period or frequency of the signal. This was made adjustable for the user of the measurement program.

### 3.5.3 Strain gauges

Standard 5 mm Kyowa 120 Ohm strain gauges of the type KFG-5-120-C1-11L3M3R were used to construct the load cell bridges on the load beams. Four gauges on each beam form two Wheatstone bridges, which are connected to two separate channels in the input module. The optimum locations for installing the strain gauges were estimated from a simulation of the beam model as seen in picture 26. The metal was machined flat around these locations and smoothed almost to a mirror finish with emery paper.

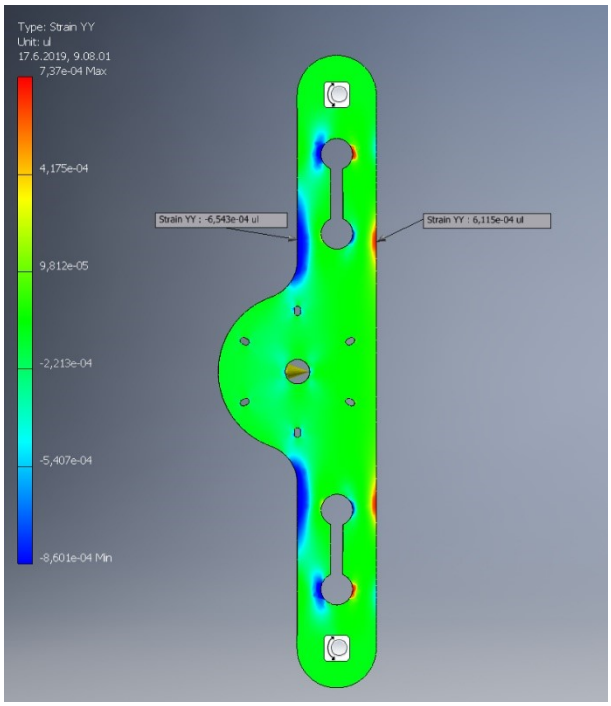


Picture 26. Finite element model simulation of the load beam.

Next the surfaces were cleaned with acetone and the gauges fixed in place with cyanoacrylate glue, then covered in a layer of protective varnish and a metal shield. The shield was not permanently fixed in place to permit inspection and replacement of the gauges. The strain gauge bridge requires an excitation voltage which is provided by the measurement input module. Each strain gauge is provided with three wires, two of which connect to the same end of the strain gauge. The extra parallel wire is used by the input module for measuring the actual excitation voltage across the bridge after any voltage losses in the wiring. The circuit diagram of the connection can be seen in picture 27.

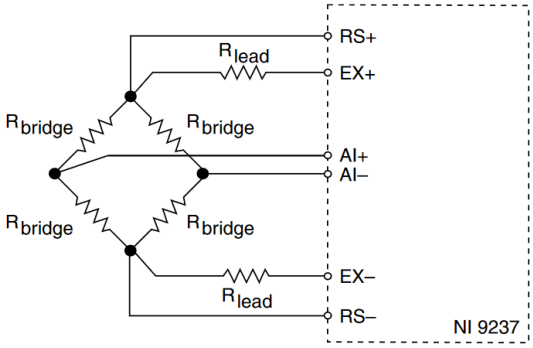


Picture 27. Circuit diagram of a load cell bridge (National Instruments 2019a).

The strain gauge input module applies an excitation voltage to the strain gauge bridge. This value can be arbitrarily chosen up to 10 Volts within the total power limits of the module. The module may reduce the voltage to limit the amount of power applied to the strain gauges (National Instruments 2019a). To compensate for the varying excitation voltage at the bridge, the output signal unit is normalized to millivolts per Volt. This reduces the measured units to parts per thousand. This is similar but not equivalent to the engineering strain units which may also be measured in parts per thousand, or parts per million known as micro-strains. mV/V is used in this document to avoid confusion.

### 3.5.4 Software

National Instruments LabVIEW 2016 Professional development environment was used for constructing and testing the measurements software. LabVIEW is a systems engineering software for control and measurement applications. It provides a graphical programming environment and a programming language consisting of logic diagrams and function blocks, as well as user interface elements for display and visualization of data. Once developed, a LabVIEW program can be deployed as stand-alone software with the correct run-time libraries and device drivers installed on the user's computer. (National Instruments 2019)

The software developed for the device sets the input module to measure all four input channels at 50,000 samples per second with a buffer or 5,000 samples. The LabVIEW program then filters the data down to a lower sample rate as specified by the user and uses this filtered data to detect high force events. Once a force event is detected, the program isolates a-specified number of data points from the signals. This data is split into measurements before, after, and during the detected force event. The strain gauge signal

is used to measure the peak of detected force. A sum integral of the strain signal over the whole captured period is used to calculate the impulse of the force. The motor channels data is split into parts to measure the wheel speeds before and after the force event. The difference in speeds is used to calculate the energy consumption from each wheel. Finally, the program tabulates the results of the calculations from the last captured data and goes back to wait for another force event to occur.

The program collects a table of measurements automatically every time the user inserts a rock into the crusher. The user may also switch the operating mode to single capture, where the program suspends data capture operations after one detected event. Once a batch of rocks has been processed, the user can save the table of results, clear the table and begin again. The program does not control the mechanism of the crusher - it simply observes its operation while the user controls the motors with the hand controller and inserts particles. The user interface also provides indicators for wheel speeds, relative speed difference, and allows the user to insert calibration constants for the measurements. The program features an automatic offset leveling function to zero the force gauges. This function is implemented as a simple proportional feedback loop that gradually approaches the correct offset value. The user may then lock the automatic offset level and force a trigger event to check that the offset is zero. If not, the user may enter a fine-tuning constant to make it zero. A screen capture of the user interface can be seen in picture 28. A diagram of the measurement program may be found in appendix 2.

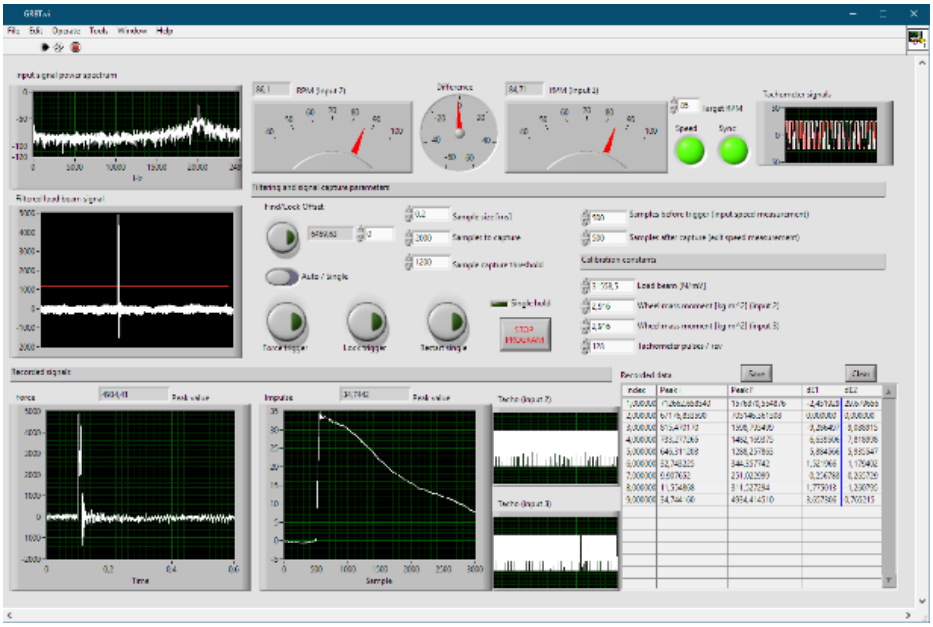

Picture 28. A screen capture of the program interface.

# 4 TESTING AND RESULTS

As soon as the wheels and frame were finished, the frame was assembled and one of the wheels was lifted in place between the frame with the workshop overhead crane. Keeping the lower frame joints loose allowed the frame to splay wide and gave easy access for assembly. The crane was used for safety reasons, although it was discovered that one person could lift the wheel without too much effort while another would insert the threaded rod through the center shaft and the frame. The load beams could be assembled around the second wheel on the shop floor and the whole movable arm with the wheel was hoisted into position in much the same manner. Although the combination of the wheel and the load beams became too heavy to lift, a single person could still assemble the whole machine with the help of some pieces of wood for ramps - by rolling the wheel into position. The parts were very heavy, but not unmanageable.

Once the wheels were in place, they could be spun easily by hand and would keep spinning for a considerable amount of time, confirming that the bearings were working as intended. With the motors installed, the magnetic drag between the rotor and the stator would stop the wheels faster and pull them to align with the magnets. The wheels were spun by hand at first without the motors installed to discover how much off-balance they were. Pieces of steel were then fixed to the inner perimeters of the wheels on both sides at the top resting position until the wheel would no longer prefer to stop at that position. The pieces were weighed, and proper counterweights were made in two pieces that were glued in on both sides of the wheel with strong epoxy.

Slight sideways runout was noted as the wheels turned, left over from the fact that the sides of the outer rings were never machined. The most likely reason for the runout is that the wheels had been fixed on the lathe very slightly askew and the center bore ended up not perfectly perpendicular to the sides. This type of symmetric imbalance would in theory cancel out in the sum of the two load beam signals. As it were, there was no noticeable shaking or vibration in the machine. Another possible reason is that the wheel blank was slightly thicker on one side, but this issue is handled by the counterweights.

Some issues with the water jet cutting process were discovered. The mounting holes for the motors were skewed slightly and had to be filed straight by hand to fit the bolts through. The mounting holes for the wheels were large enough but provided a different

issue: the center shaft could sit a millimeter and a bit lower than intended because of the relaxed tolerances. This would cause the motors to bind up, and since the stator could not easily move without more filing, cylindrical shims were rolled out of 0.5 mm sheet steel and inserted around the threaded rod through the wheel center shaft. This centered the wheel to its mounting holes and aligned the motors.

With everything aligned in place, the threaded rods and nuts were tightened with enough torque to keep the joint by friction. The clamping force was chosen to be 100 kN. Assuming a static coefficient of friction of 0.7 between the parts, this would hold the full 70 kN of shearing force applied to one end of the wheel shaft, for a safety factor of two when the load is evenly distributed. The required torque was estimated between 250–400 Nm for the properties of standard dry zinc plated M30 threads (Airila et al. 2003, pp. 228–234). The tightening torque was supplied by an 85 kg person applying their weight on a wrench with half a meter of leverage, producing at least 400 Nm. About half as much torque would be required to close the adjustment link when changing the gap size. The unknown and potentially varying amount of friction between the thread meant that no precise amount of clamping torque could be given – instead the load beam was simply tightened by hand-feel and re-tightened if the gap started to slip during measurements. No slipping was observed after getting a feel for the appropriate tightness.

The first operation on the fully assembled device was determining the load beam force coefficient. The model simulations of the load beam indicated that the relationship between force and strain in the sensor locations would be linear, so a reasonable calibration coefficient could be produced by loading the system with enough force and observing the signal output at different test loads. A load placed on the wheel divides linearly between the two halves of the device, so the measured signal value was taken as the sum of both load beam signals. This helps to reduce any uncorrelated noise in the signals. A single calibration coefficient was then applied to the sum to convert the signal value into force. Although the beams have slightly different properties, if the forces are mostly centered, the resulting error should be small. The two load beams will necessarily have slightly different calibration coefficients, and the sum signal is the average of them.

The workshop overhead crane was used as a heavy pendulum to pull on the adjustment link arm. A digital scale was attached to the link arm and a steel cable tied horizontally from the scale to the crane hook. The mechanical leverage of the load beam causes twice the force against the wheel, so the scale readings were doubled and converted to the force $F_{Gap}$ by multiplying with the gravitational constant 9.81 m/s$^2$. The crane was moved slowly away from the crusher to offset the pendulum and left to rest against the steel cable. Three measurements listed in table 3. were made with the pendulum offset by different amounts, reading up to 36.55 kg on the scale. The maximum capacity of the scale was 40 kg. The results can be seen plotted in picture 29. with a linear trend intersecting at zero.

Table 3. Load beam calibration measurements.

| # | d mV / V | [kg] | $F_{Gap}$ [N] | F / mV / V |
|---|---|---|---|---|
| 0 | 0 | 0 | 0 | - |
| 1 | 0.00725 | 11.67 | 228.90 | 31572.41 |
| 2 | 0.01604 | 24.46 | 479.90 | 29918.95 |
| 3 | 0.02161 | 36.55 | 717.11 | 33184.17 |
| Average | | | | 31558.51 |

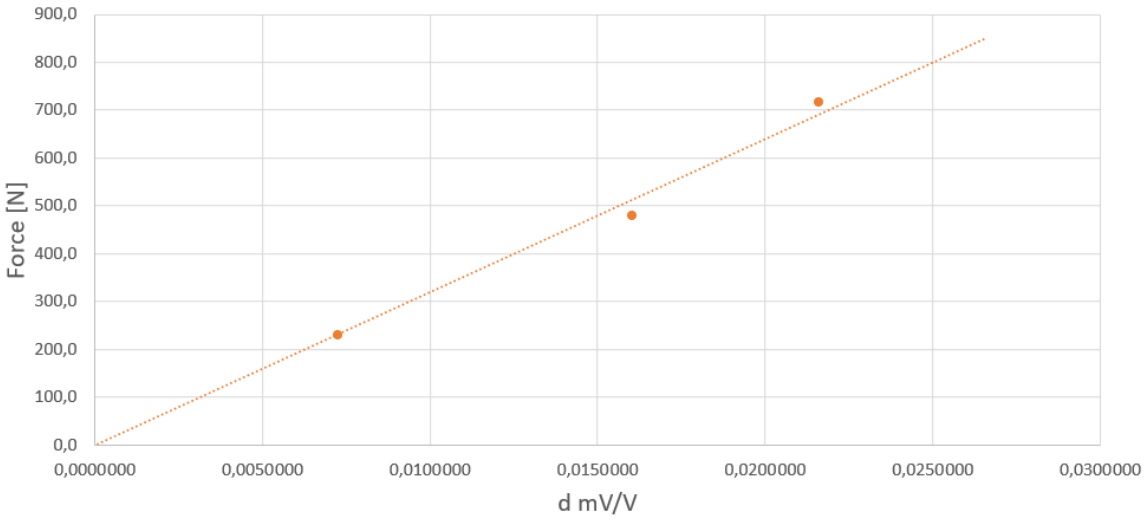


Picture 29. Calibration measurement data points with a linear trend.

The method of calibration was found difficult to perform because the machine had to be moved to allow more room to swing the crane and the scale would reset itself periodically. The measuring program was zeroed for offset between each measurement. The average of the three results was used for the load beam coefficient. Another way of calculating the coefficient would be to treat zero as one data point and observe a linear trend between the values. This method gives a value of 32430 F/mV/V which is 2.7 % larger. The differences might be explained by residual errors and noise in the zero offset of each measurement, which is why the averaged slope from zero to each data point was used instead. The results appear to line up well with the prediction that the load beam is behaving linearly, although greater forces could not be tested. The main interest from the device for breakage testing purposes is the energy estimation, which is measured directly and independently of the force, so the calibration of the load beams may be refined later.

The wheel moment of inertia coefficient for computing the energy of comminution was taken as reported by the CAD software. The wheel and bearings without a motor count for 2.870 kg-$m^2$. The 200 g counterweight added to each wheel, revolving around a radius of 480 mm adds 0.012 kg-$m^2$. The motor part was estimated as a 1.5 kg thin ring with a diameter of 300 millimeters, adding another 0.034 kg-$m^2$ for a total of 2.916 kg-$m^2$.

For the first tests the sampling parameters were set to a minimum threshold of detection at 1200 Newtons. A lower threshold could be used, but an intermittent source of electrical noise was found to produce false triggers once or twice a minute. The power supply unit was also producing strong electrical noise at just above audible frequencies. To reduce the probability of false triggers and to reduce electrical noise in the signal, the data sample time was set at 0.2 milliseconds. The data samples to be captured were set at 2000 for 400 milliseconds of data per event. Additional 500 data samples were captured before the force trigger to measure the initial speed of the wheels over a period of 100 ms, and 500 data samples from the end of the recorded data were used to measure the exit speed. The program was set to average the speed signal over two cycles of the speed signal waveform, corresponding to two teeth on the encoder wheel. This was to ensure that the program could measure the speed signals all the way down to 10 RPM where the remaining energy in the wheels would be 3 Joules.

The first test was conducted with particles of a nominal size of 20 millimeters. The size reduction at the gap was selected to be 4:1, 4:2 and 4:3 to produce distinct crushing energy levels for 30 particles at each level. The fragments and fines produced by breakage were collected in a tray under the crusher wheels and separated according to mine location and gap size. The material consisted of medium to hard rocks from different mine sites around Finland at Sodankylä, Kittilä, Polvijärvi and Sotkamo. The sample material was provided by Tabatha Chavez Matus as part of her thesis work in parallel with the prototype development. The tests were conducted in collaboration to produce data for her thesis.

The device was set up at 60 RPM and 114 Joules of energy. The wheels were allowed to reach the set speed, then the motors were switched off to cut torque to the. Immediately after switching the motors off, the particle was dropped between the wheel gap. The drop height was calculated according to the free fall speed of the particle to match the surface speed of the wheels. After the measurement was recorded, the motors were turned back on and the process was repeated. The first particle failed to pass through a 5 mm gap and blocked the device, so the speed was increased to 85 RPM and the energy to 231 Joules. The rest of the particles were broken without blockages. A small number of particles passed through without registering enough force to trigger a measurement. This would typically happen at the largest gap opening. After some practice, the time to process a bag of 30 particles was estimated to take approximately five minutes.

All the collected data for all the mines and gap sizes for the first test of 20 mm particles are condensed for display in picture 30. This graph shows the relationship between the measured peak force in Newtons and the impulse of the force in Newton-Seconds. The choice of a power function to represent different trends at different gap sizes was made according to best fit to the data out of the available options in Microsoft Excel. The width of each bubble is proportional to the amount of comminution energy measured for the particle. The highest energy measured in the set was just under 200 Joules. This was found at the 4:1 gap reduction ratio.

The correlation between the measured comminution energy and the impulse and force for the 20 mm particle data can be seen in picture 31. No data exists below the minimum detection threshold of 1200 N. The highest force measured was 56 kN. An illustration of the distributions of energy for the different gap sizes can be seen in picture 32.

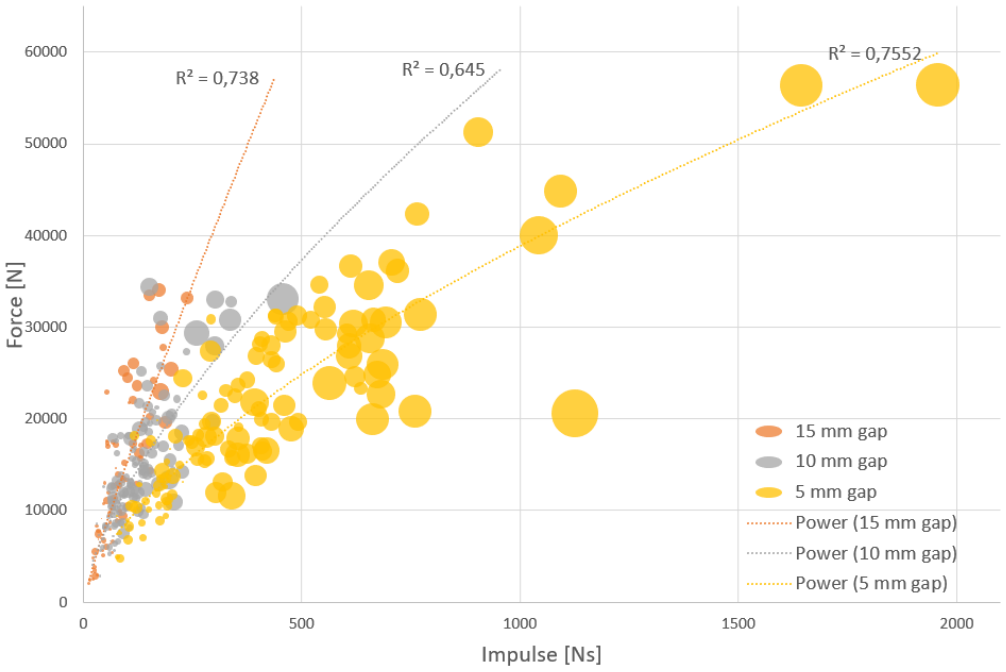


Picture 30. Force, impulse and energy for a sample of 20 mm particles


Picture 31. Correlations between energy and impulse, force, in the full sample.

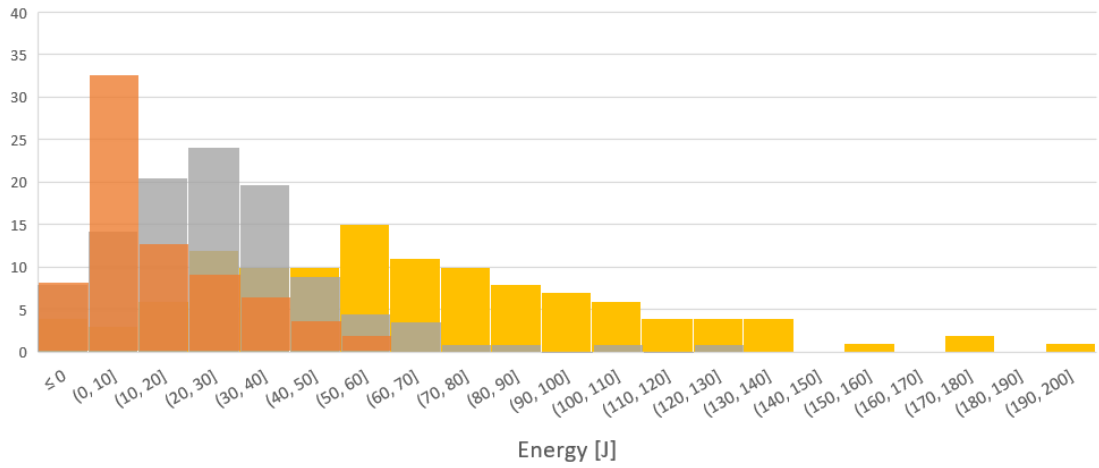


Picture 32. Distributions of energies in the full sample.

Preliminary data and the broken samples of the initial test on 20 mm particles were collected and processed by Tabatha Chavez Matus. The measured $t_{10}$ of each sample at the measured energy level of that sample was compared against a $t_{10}$ curve predicted by a commercial Drop Weight Test on a control sample taken out of the same lot. The results provided in picture 33. show a good agreement between the two tests, despite of some issues in the accuracy of the energy estimation in the GRBT measuring software that were discovered along the way.

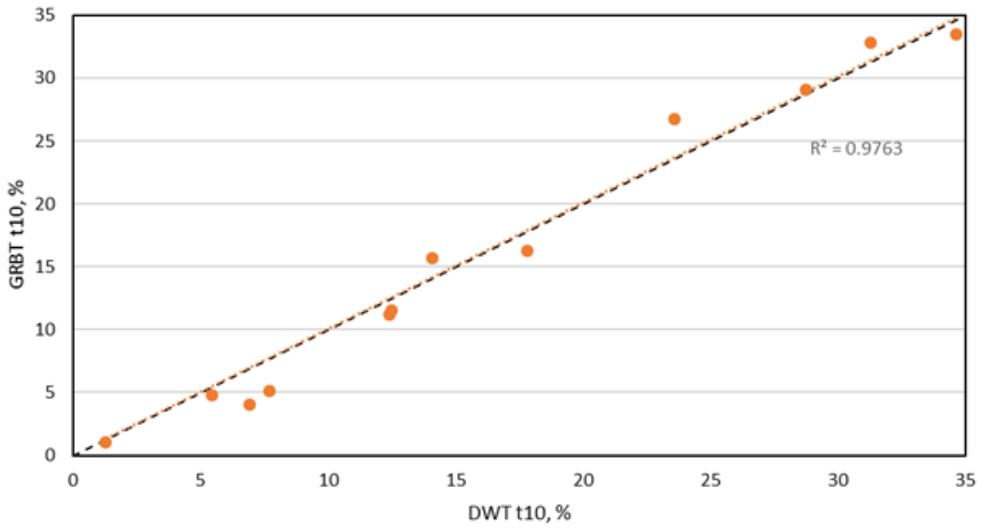


Picture 33. GRBT and DWT measured versus predicted $t_{10}$ (Chavez Matus 2019).

The first test proved that the device was functional, and measurements could be made. More tests were scheduled and performed with different types and sizes of rocks. The

largest particles tested in the device were nominally 29 millimeters in size. The gap size was adjusted to 13, 18 and 22 millimeters and 30 particles were passed through at each gap opening. The sample size separation process was found to produce particles with elongated shapes. These elongated particles would typically break into two or more pieces and the separated part would shoot upwards and fall back into the gap a few milliseconds later. These multiple breakage events appeared in the same captured data or caused a second event capture immediately afterwards. The elongated rocks consumed more energy simply by having more material to break and the wheels would stop on the late fragments that fell back into the gap. When this was discovered, the rest of the 29 mm particles in the sample were sorted by shape and the most elongated rocks were removed from the selection. The more evenly shaped particles were passed through without issues.

The device was also measured without any particles passing through. The motors were turned off and immediately afterwards a manual trigger was used in software to record the energy loss of the wheels themselves. 20 measurements were taken, and the amount of energy lost to friction and magnetic drag was estimated at 7 Joules for each wheel. This number was subtracted from the data of the measured energy level to derive the true comminution energy. Closer examination of the wheel energy loss data revealed a problem with the measuring program. The program was not measuring the average period of the encoder signal pulses over the recorded data, but only a single pulse period found before and after the crushing event. The problem was found to be caused by a simple misunderstanding of the LabVIEW programming documentation. When the wheels were turning at their highest speed, this programming error would cause the energy measurement to round up to increments of 6 – 8 Joules.

The difference in wheel speed for a given difference in energy becomes smaller at greater speeds, so the relative accuracy of the measurement for low energy events turned out to be very poor. The method of measurement was changed from computing the time period of an on-off pulse cycle to computing the fundamental signal frequency over the recorded data period by an interpolated Fourier Transform program function. The no-load energy consumption of the device was measured again with the new method using the same sampling parameters as previously. The mean no-load energy consumption was calculated at 13.51 Joules with a standard deviation of 1.07 Joules over 10 measurements. This gives the device a mean power consumption of 33.8 Watts including both the magnetic drag of the motors and the friction of the bearings. Leaving the motors on to

reduce the energy loss was considered as an option and tried, but the electrical noise caused by the motor controllers was found to interfere noticeably with the load beam signal. The amount of torque produced by the motor is not entirely steady and the motor controller program will intervene automatically with a delay of some few milliseconds on detecting the loss of speed. This means the amount of energy added by the motors during the breakage event would vary unpredictably if they were not turned off.

During the testing, some minor loss of fine materials was observed. The broken particles tended to produce dust that was carried away by air currents. While the particles did generally eject downwards from the gap, some small amount of material would get stuck to the wheels and carried around, and on few occasions a particle would break with such force that the fragments would rebound past the collection tray or fly up towards the operator. In some of these cases, a larger shard or fragment would bounce around and get stuck in the narrow gap between the side of the wheel and the drop chute wall, dragging and grinding against the wheel until the device was stopped and the fragment removed. A series of high-speed photographs of a typical breakage event taken through an opened hatch on the side of the machine can be seen in picture 34. The series shows the particle breaking in two distinct parts while passing through the gap with a spray of dust and fragments ejected below. This series was taken with a Sony Cyber-shot DSC-RX100 IV camera lent by the Oulu Mining School. The individual frames were cropped and combined into a single image.

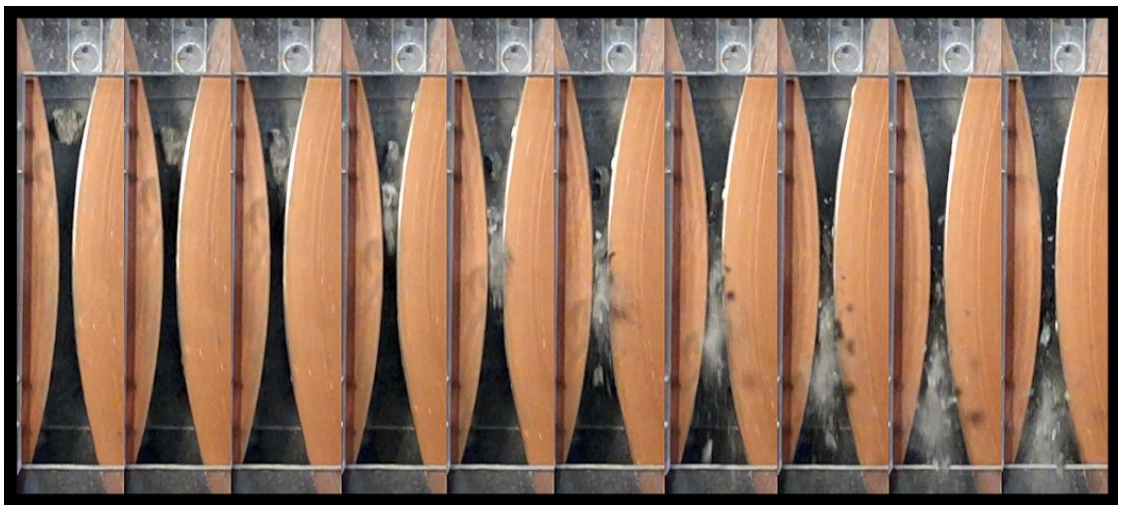

Picture 34. A particle breakage event in a series of high-speed photographs.

# 5 DISCUSSION AND ANALYSIS

The data collected with the device shows measurable differences between energy levels at different gap settings. Full validation of the measurement data is still underway at the time of writing of this thesis, and more trials are needed for a proper comparison with the other test methods. While the energy level cannot be controlled as precisely as in the Drop Weight Test, or the Split Hopkinson Bar Test, it can be varied to produce different levels of breakage which is necessary for fitting the parameters of the comminution curve in equation (1). Instead of choosing the amount of energy to put in, the device is measuring the energy applied, which serves the same purpose.

The main limitation of the technique is with the accuracy and precision of measuring the comminution energy. The linear trend between energy and impulse of force seems to suggest a small residual offset in the energy measurement, even after accounting for the friction losses in the wheels. Some residual energy offset is expected to happen, because the force of friction in the bearings depends on the load on the wheel which increases at the instant of particle breakage. The amount of friction in the bearings cannot be accurately known in advance because it depends on various factors such as temperature, the condition of the bearings, the lubrication of the bearings, and other effects. However, since the loss of energy to friction is proportional to the load, this error should correlate with the amount of impulse and energy being measured. The correlation is not perfect since the amount of energy lost to friction is a function of the radial force and the amount of rotation of the wheels - not force over time. Likewise, observing the energy alone does not indicate how much the wheels had to turn to apply that energy. Perfecting the result is not necessary if the error can be reduced enough to be useful. A simple linear function may be used to subtract more energy when a higher impulse is detected. A combination of the measured variables might be used to create a correction function that reduces the energy value by an appropriate amount.

For the purpose of modelling the comminution behavior of rock in a roll crusher, leaving the energy consumed by the bearings in the results produces a characteristic difference in comparison to the other tests which do not replicate these circumstances - so this error may not be an error but a feature.

If the force and impulse measurements are to be used for normalizing the results, the load beam calibration coefficient and method of measurement should be refined further. Both beams should be calibrated independently and a better method of applying the calibration force should be developed. Existing attachment points on the device frame could be used to hold a bracket to pull on the link arm with a screw. The device is measuring the force of separation between the crushing wheels along one dimension, so the exact radial force on the wheel is unknown. The load beam could be re-designed to measure forces along a plane, revealing the direction and magnitude of the force. This would also indicate the amount of rotation of the wheel by the rotation of the force vector, and this information could be used to calculate both the energy lost to the bearings and the remainder that applies to the particle. On the other hand, a more advanced version of the measuring program might scan the captured speed signal data and compute the frequency at each point in time. Integrating the speed signal would gain information about the wheel angle during the breakage event. Since the particles are small compared to the wheels, the difference between the force of separation and the true radial force on the wheels is small as well. Assuming the two are the same causes a slight error, but since this error would apply to the small increase in energy lost to the bearings under load, the relative error to the whole measurement is most likely negligible.

The present means of using optical encoders and measuring a difference in stored energy before and after particle breakage is fundamentally sound, but the implementation needs refinement. A better optical encoder wheel with improvements in the measuring software would improve on the resolution and provide more data points. The use of Discrete Fourier Transforms works best when measuring a continuous waveform with a stable frequency over the sampling period (Jain et al. 1979), so this method does not provide much useful information during the time when the wheel speeds are changing rapidly. A truly continuous measurement of the wheel speed would require a different type of sensor. The true moment of inertia of the wheels could also be characterized to a greater accuracy by observing the deceleration of the wheel with and without an additional mass. If the friction forces are considered to be linear, the comparison can be used to cancel out the terms of friction from the calculation.

The device is certainly quick to operate and as the particles pass through the gap there is no later re-breakage, nor the possibility of a premature particle breakage, avoiding some of the potential issues present in the other comminution tests. The potential loss of fine

material from the breakage products is a concern because the whole test is based on estimating the mass ratio of the finer particles passing through a sieve. However, an alternative way of measuring the breakage products is to observe the mass of particles which do not pass the sieve because they are greater in size. This yields the same information and solves the problem of finer particles and dust escaping the collection tray or sticking to the wheel surfaces. The problem of the dust ending up inside the bearings and in the optical encoders remains, so better sealing of the wheel hubs should be provided. A fan and a filter to could be provided to remove the dust from the device and from being inhaled by the operator. The use of inductive or capacitive encoders instead of the optical gate would provide resilience against dust accumulation in the sensor.

As a conclusion; this project was conducted to design, build and test a functioning prototype device for measuring the comminution of rock particles. Based on the measurements and data collected on the device so far, the device meets its basic requirements and specifications despite some minor compromises in its construction. It has the potential to be improved for greater accuracy and precision with further refinement of both hardware and software.

# 6 SUMMARY

This thesis presents a new testing device built as a proof of concept for a new comminution test for measuring the breakage characteristics of rock particles. The prototype device was commissioned as a part of a project to develop a fast, low-cost, and reliable breakage characterization test for geo-metallurgical modelling. The work was done in collaboration between the Oulu Mining School and the Mechatronics and Machine Diagnostics Research Group in the University of Oulu.

Mining has been one of the cornerstones of human civilization and one of the key processes involved in minerals extraction is comminution. Mineral ores are broken down to smaller particles with various kinds of crushing and grinding machinery in order to liberate the materials of interest. Comminution testing can be used for mapping the properties of rocks in mine sites for the purposes of optimizing these processes. A selection of such tests used by the industry includes the Drop Weight Test, The SAG Mill Comminution test, The Ultra-fast Load Cell Device, the Twin Pendulum test, the Split Hopkinson Bar Test, and the Rotary Breaker Test. In addition to these commonly used tests, various instrumented versions of actual crushing equipment may be used. In these testing methods, rock particles are subjected to varying levels of impact energy and the amount of fine materials liberated by breakage is measured against the energy input.

The role of mechatronic engineering in this context of comminution testing equipment is to design and develop intelligent machines that ease the work of the researchers and technicians who use the devices. Instead of being simple measuring tools and instruments that require skillful handling, a mechatronic device works with the principles of feedback from sensors and information processing systems to adjusts itself to the demands of the task.

The structure of the new device was proposed as a variation of an instrumented roll crusher with an adjustable gap. The applied energy level would be chosen by the size reduction ratio of the crusher by varying the gap size relative to the size of particles in a range of 16 - 50 mm. The available energy would range between 100 – 250 Joules. The resulting design of a double wheel crusher included a pair of narrow steel wheels 600 millimeters in diameter, powered by integrated brushless electric motors between an adjustable steel frame. Sensors built into the adjustable frame provide data about the impact forces, and encoders on the wheels measure their loss of rotation to determine the

energy input into each tested particle. The particles are inserted from the top of the device and the breakage products collected from a tray placed on a shelf at the bottom. Data acquisition hardware from National Instruments is used to record each breakage event automatically, allowing the operator to insert particles one after the other.

The main work of designing, building and testing the device was conducted during the spring and summer of 2019. After completing the assembly and preliminary calibrations, the first trial operation of the prototype was made using medium to hard rocks from different mine sites around Finland at Sodankylä, Kittilä, Polvijärvi and Sotkamo. The test set resulted in data with clearly identifiable levels of energy and correlations between the measured amounts of force and impulse on the rock particles. The energy of breakage for 20 mm particles was found to reach a maximum of 200 Joules at a reduction ratio of 4:1. The highest force of breakage measured was 56 kilonewtons.

Some issues were found with the accuracy of energy measurements due to errors in data processing. The programming error behind the fault was corrected and the device was tested to produce a standard deviation of measurement of 1.07 Joules in a no-load condition. Means to improve the accuracy of the energy and force measurements were discussed, with recommendations and suggestions for other improvements to the device in the future. The present means of using optical encoders and measuring a difference in stored energy before and after particle breakage is fundamentally sound, but the implementation requires refinement.

The results show that the device is functional and meets or exceeds the requirements given in the specifications, proving that the concept is plausible and can be developed further. More extensive testing is required for proper comparison with the other test methods and validation of the data.

# BIBLIOGRAPHY

Acar M., Parkin R.M., 1996. Engineering education for mechatronics. IEEE Transactions on Industrial Electronics, 43(1), pp. 106-112. Available from: https://doi.org/10.1109/41.481414

Airila M., et al. 2003. Koneenosien suunnittelu. 4th edition. WS Bookwell Oy. ISBN 951-0-20172-3.

Altindag R., Guney A., 2010. Predicting the relationships between brittleness and mechanical properties (UCS, TS and SH) of rocks. Scientific Research and Essays, 5(16), pp. 2107-2118. Available from: https://academicjournals.org/journal/SRE/article-full-text-pdf/A577CD017017

Chandra S., Ismail A. B. Md, 2009. PC sound-card based simple instrument for the potentiometric sensors. Sensors and Actuators A: Physical, 154(1), pp. 65-68. Available from: https://doi.org/10.1016/j.sna.2008.11.002

Chandramohan R., Lane G.S., Foggioatto B., Bueno M.P., 2015. Reliability of some ore characterization tests. 6th International Autogenous and Semi-Autogenous Grinding Technology, Vancouver, September 2015. Available from: https://www.researchgate.net/publication/323218453_Reliability_of_some_ore_characterization_tests

European Union, 2006. Directive 2006/42/EC of the European Parliament and of the Council of 17 May 2006 on machinery and amending Directive 95/16/EC. EUR-Lex. Available from: https://eur-lex.europa.eu/eli/dir/2006/42/oj

Grady D.E., Lipkin J., 1980. Criteria for Impulsive Rock Fracture. Geophysical Research Letters, 7(4), pp. 255-258. Available from: https://doi.org/10.1029/GL007i004p00255

Honeywell, 2019. Hall Effect Sensing and Application. Technical Information [Online document]. Available from: https://sensing.honeywell.com/hallbook.pdf [Accessed 10.12.2019]

Hsu T.-R., 1997. Mechatronics — An Overview, IEEE Transactions on components, packaging, and manufacturing technology - Part C, 20(1). Available from: https://doi.org/10.1109/3476.585138

Jain V. K., Collins W. L., Davis D. C., 1979. High-Accuracy Analog Measurements via Interpolated FFT. IEEE Transactions on Instrumentation and Measurement, 28(2), pp. 113-122. Available from: https://doi.org/10.1109/TIM.1979.4314779

Landau H. J., 1967. Sampling, data transmission, and the Nyquist rate. Proceedings of the IEEE, 55(10), pp. 1701-1706. Available from: https://doi.org/10.1109/PROC.1967.5962

Legendre D., Zevenhoven R., 2014. Assessing the enrgy efficiency of a jaw crusher. Energy, 74, pp. 119-130. Available from: http://dx.doi.org/10.1016/j.energy.2014.04.036

Lieberwirth H., Hillmann P., Hesse M., 2017. Dynamics in double roll crushers. Minerals Engineering, 103-104, pp. 60-66. Available from: http://dx.doi.org/10.1016/j.mineng.2016.08.009

Liu S., Xu J., 2013. Study on dynamic characteristics of marble under impact loading and high temperature. International Journal of Rock Mechanics and Mining Sciences, 62, pp. 51-58. Available from: http://dx.doi.org/10.1016/j.ijrmms.2013.03.014

Mazur M., Mikova K., 2016. Impact resistance of High Strength Steels. Materials Today: Proceedings, 3(4), pp. 1060-1063. Available from: https://doi.org/10.1016/j.matpr.2016.03.048

McKen A., Williams S., 2005. An Overview of the Small-Scale Tests Available to Characterize Ore Grindability for Design Purposes. SGS Technical Paper #2005-06. Available from: https://www.sgs.com/-/media/global/documents/technical-documents/sgs-min-tech-pub-2005-06-small-scale-tests-lr-en-11-09-v1.pdf

Morris W.G., 1994. Measuring the strength of abrasive grains. US Patent application US5392633A.

Mwanga A., Rosenkranz J., Lamberg P., 2015. Testing of Ore Comminution Behavior in the Geometallurgical Context—A Review. Minerals, 5(2), pp. 276–297. Available from: http://dx.doi.org/10.3390/min5020276

National Instruments, 2019. Shop, What is LabVIEW? [Online document]. Available from: https://www.ni.com/fi-fi/shop/labview.html [Accessed 1.12.2019]

—— 2019a. Datasheet NI 9237 [Online document]. Available from: https://www.ni.com/pdf/manuals/374186a_02.pdf [Accessed 1.12.2019]

—— 2019b. Support, NI Product Manuals, CompactDAQ Chassis Manual [Online document]. Available from: https://www.ni.com/documentation/en/compactdaq-chassis/latest/cdaq-9171/overview/ [Accessed 1.12.2019]

—— 2019c. User Guide NI 9949 RJ-50 to Screw-Terminal Accessory [Online document]. Available from: https://www.ni.com/pdf/manuals/372278b.pdf [Accessed 1.12.2019]

Nogychi T., Watanabe M., 1992. Apparatus for measuring grindability of powder material. US Patent application US5133209A.

Refahi A., Aghazadeh Mohandesi J., Rezai B., 2010. Discrete element modeling for predicting breakage behavior and fracture energy of a single particle in a jaw crusher. International Journal of Mineral Processing, 94(1-2), pp. 83-91. Available from: https://doi.org/10.1016/j.minpro.2009.12.002

Sen P.C., 1990. Electric motor drives and control-past, present, and future. IEEE Transactions on Industrial Electronics, 37(6), pp. 562-575. Available from: https://doi.org/10.1109/41.103462

Shannon C.E., 1949. Communication in the presence of noise. Proceedings of the IRE, 37(1), pp. 10–21. Available from: https://doi.org/10.1109/JRPROC.1949.232969

SKF Group, 2019. Products, Bearings, units and housings, Principles of rolling bearing selection [Online document]. Available from: https://www.skf.com/group/products/bearings-units-housings/principles/index.html [Accessed 1.12.2019]

—— 2019a. Needle roller bearings, with machined rings, with an inner ring, NA 4912 [Online document]. Available from: https://www.skf.com/group/products/bearings-units-housings/roller-bearings/needle-roller-bearings/needle-roller-bearings-with-machined-rings/with-machined-rings-w-inner-ring/index.html?designation=NA%204912 [Accessed 1.12.2019]

—— 2019b. Cylindrical roller bearings, double row, full complement, NNCL 4912 CV [Online document]. Available from: https://www.skf.com/group/products/bearings-units-housings/roller-bearings/cylindrical-roller-bearings/double-row-full-complement-cylindrical-roller-bearings/double-row-full-complement/index.html?designation=NNCL%204912%20CV [Accessed 1.12.2019]

—— 2019c. Product, Bearings, units and housings, Principles of rolling bearing selection, Bearing selection examples, Supporting wheel [Online document]. Available from: https://www.skf.com/group/products/bearings-units-housings/principles/bearing-selection-examples/supporting-wheel/index.html [Accessed 1.12.2019]

Spitz K., Trudinger J., 2019. Mining and the Environment: From Ore to Metal. 2nd Edition. CRC Press. 796 p. ISBN 1351183656, 9781351183659. Excerpt available from: https://books.google.fi/books?hl=fi&lr=&id=oWytDwAAQBAJ [Accessed 14.1.2020]

SSAB, 2019. Products, Raex(r) 450 [Online document]. Available from: https://www.raexsteel.com/products/450 [Accessed 1.12.2019]

Trinamic, 2019. Products, Modules, TMCM-1640 [Online document]. Available from: https://www.trinamic.com/products/modules/details/tmcm-1640/ [Accessed 1.12.2019]

—— 2016. TMCM-1640 TMCL Firmware V2.08 Manual (Rev. 2.04 / 2016-FEB-16) [Online document]. Available from: https://www.trinamic.com/fileadmin/assets/Products/Modules_Documents/TMCM-1640_TMCL_firmware_manual.pdf [Accessed 12.12.2019]

Tromans D., 2008. Mineral comminution: Energy efficiency considerations. Minerals Engineering, 21(8), pp. 613-520. Available from: https://doi.org/10.1016/j.mineng.2007.12.003

Tsotoulidis S., Safacas A., 2014. Side-effects of Hall sensors misplacement on BLDC motor drive operation. 2014 International Conference on Electrical Machines (ICEM), Berlin, 2014, pp. 1825-1830. Available from: https://doi.org/10.1109/ICELMACH.2014.6960431

Urquizo A, 2011. PID controller overview [Online document]. Wikimedia commons. Available from: https://commons.wikimedia.org/wiki/File:PID_en.svg [Accessed 1.12.2019]

Whittles D.N., Kingman S., Lowndes I., Jackson K., 2006. Laboratory and numerical investigation into the characteristics of rock fragmentation. Minerals Engineering, 19(4), pp. 1418-1429. Available from: https://doi.org/10.1016/j.mineng.2006.02.004

Yan F., Feng XT., Chen R., Xia K. Jin C., 2011. Dynamic Tensile Failure of the Rock Interface Between Tuff and Basalt. Rock Mechanics and Rock Engineering, 45(3), pp. 341-348. Available from: https://doi.org/10.1007/s00603-011-0177-y

Yedamale P., 2003. AN885 Brushless DC (BLDC) Motor Fundamentals [Online document]. Available from: http://ww1.microchip.com/downloads/en/AppNotes/00885a.pdf [Accessed 1.12.2019]

Zhang Z., 2004. Estimate of loading rate for a TBM Machine Based on Measured Cutter Forces. Rock Mechanics and Rock Engineering, 37(3), pp. 239-248. Available from: https://doi.org/10.1007/s00603-004-0025-4

Zhang Z.X., Kou S.Q., Jiang L.G., Lindqvist P.-A, 2000. Effects of loading rate on rock gracture: fracture characteristics and energy partitioning. International Journal of Rock Mechanics and Mining Sciences, 37(5), pp. 745-762. Available from: https://doi.org/10.1016/S1365-1609(00)00008-3

Attachment 1. An example of a motor control program written in TMCL.

```
//=== module settings for axis 0 ===
SAP 134, 0, 2                // current regulation loop delay [50us]
SAP 6, 0, 5000               // max current [mA] (peak)
SAP 25, 0, 60000             // thermal winding time constant [ms]
SAP 26, 0, 960000            // IIt limit
SAP 172, 0, 6000             // torque P
SAP 173, 0, 0                // torque I
SAP 177, 0, 4000             // start current [mA] (peak)
SAP 245, 0, 0                // overvoltage protection
SAP 133, 0, 1                // velocity regulation loop delay [ms]
SAP 4, 0, 150                // max velocity [rpm]
SAP 7, 0, 0                  // target reached velocity [rpm]
SAP 9, 0, 1                  // motor halted velocity [rpm]
SAP 10, 0, 1                 // target reached distance
SAP 146, 0, 0                // velocity ramp on/off
SAP 11, 0, 600               // acceleration ramp [rpm/s]
SAP 234, 0, 65000            // velocity P
SAP 235, 0, 0                // velocity I
SAP 159, 0, 6                // commutation mode (0,6,8)
SAP 253, 0, 36               // motor poles
SAP 254, 0, 0                // hall sensor invert
SAP 252, 0, 0                // hall interpolation
SAP 164, 0, 0                // activate stop switch
SAP 166, 0, 0                // stop switch polarity
SAP 241, 0, 10               // init velocity [rpm]
SAP 244, 0, 100              // init sine delay [ms]
SAP 249, 0, 1                // init sine mode
//Main function
Main:

Loop:                        //Main loop
GIO 1, 0                     //read in limit switch 1
JC ZE, Halt                  //if zero then stop the motor
GIO 0, 0                     //read in limit switch 0
JC ZE, Lo                    //if zero then switch to alternative tuning
SAP 234, 0, 35000            // velocity P
SAP 235, 0, 350              // velocity I
Cont:
GIO 0, 1                     //read ADC_IN_0 to accumulator
CALC DIV, -17                //divide accumulator by -17
AAP 2, 0                     //accumulator to target velocity [rpm]
CALCX LOAD                   //accumulator to X register
GAP 3, 0                     //get actual velocity [rpm]
CALCX SUB                    //subtract X register from accumulator
COMP -2                      //compare accumulator value to -2.
JC LE, Led                   //If speed is reached, turn LED on
SIO 0, 2, 0                  //else turn LED off
Return:
JA Loop                      //Main loop end


Lo:                          //Switch to alternative tuning
SAP 234, 0, 60000            // velocity P
SAP 235, 0, 100              // velocity I
JA Cont                      // return to Main


Halt:                        //Stop the motor
SAP 155, 0, 0                //set torque to zero
SIO 0, 2, 0                  //turn off LED
GIO 1, 0                     //read in limit switch 1
JC ZE, Halt                  //if zero then keep halting
JA Main                      //Return to main

//Turn on LED and jump back
Led:
SIO 0, 2, 1                  //Turn on LED
JA Return

STOP
```

Attachment 2. LabVIEW program diagram of the GRBT measurement program